Electrochemical and Computational Analysis of Thiocolchicoside as a New Corrosion Inhibitor for Biomedical Ti6Al4V Alloy in Saline Solution: DFT, NBO, and MD Approaches

Inam M.A. Omar , Ibrahim Elshamy , S.A. Halim , Magdy Ibrahim *

Posted Date: 12 September 2025

doi: 10.20944/preprints202509.1018.v1

Keywords: thiocolchicoside drug; corrosion inhibitor; Ti6Al4V; MD simulation; DFT; NBO

Article

Electrochemical and Computational Analysis of Thiocolchicoside as a New Corrosion Inhibitor for Biomedical Ti6Al4V Alloy in Saline Solution: DFT, NBO, and MD Approaches

Inam M.A. Omar [1], Ibrahim H. Elshamy [2], Shimaa Abd El Halim [3] and Magdy A. M. Ibrahim [2,*]

[1] Department of Chemistry, College of Science, Taibah University, Al Madinah Al Munawara 30002, Saudi Arabia

[2] Department of Chemistry, Faculty of Science, Ain Shams University, Abbassia, Cairo 11566, Egypt

[3] Department of Chemistry, Faculty of Education, Ain Shams University, Roxy 11711, Cairo, Egypt

* Correspondence: magdyibrahim@sci.asu.edu.eg

Abstract

The Ti6Al4V alloy is considered the most beneficial of the titanium alloys for use in biomedical applications. However, it corrodes when exposed to various biocompatible fluids. This investigation aims to evaluate the corrosion inhibition performance of the Ti6Al4V in a saline solution (SS) using thiocolchicoside (TCC) drug as an environmentally acceptable corrosion inhibitor. The corrosion assessments were conducted using potentiodynamic polarization curves (PPCs), open-circuit potential (OCP), and electrochemical impedance spectroscopy (EIS) methodologies, supplemented by scanning electron microscopy (SEM), energy-dispersive X-ray (EDS) analysis, atomic force microscopy (AFM), and contact angle (CA) measurements. The outcomes indicated that the inhibitory efficacy improved with higher TCC concentrations (achieving 92.40% at 200 mg/l of TCC) and diminished with an increase in solution temperature. TCC's physical adsorption onto the surface of the Ti6A14V, which adheres to the Langmuir adsorption isotherm, explains its mitigating power. The TCC acts as a mixed-type inhibitor. The adsorption and inhibitory impact of TCC were examined at various temperatures using PPC and EIS. When TCC is present, the corrosion's apparent activation energy is higher (35.79 kJ mol^{-1}) than when it is absent (14.46 kJ mol^{-1}). In addition, the correlation between the structural properties of thiocolchicoside (TCC) and its corrosion inhibition performance was systematically analyzed. Density Functional Theory (DFT) calculations were utilized to characterize the adsorption mechanism, supported by Natural Bond Orbital (NBO) analysis and Molecular Dynamics (MD) simulations. The combined computational and electrochemical findings confirm that TCC provides effective and enhanced corrosion protection for the Ti6Al4V alloy in a saline environment. These characteristics provide compelling evidence for the suitability of these pharmaceutical compounds as promising corrosion inhibitors.

Keywords: thiocolchicoside drug; corrosion inhibitor; Ti6Al4V; MD simulation; DFT; NBO

1. Introduction

The high strength-to-mass ratio and biocompatibility of titanium alloys, which include corrosion resistance, make them desirable alloys [1]. These advantages have led to several applications in biomedical implants, including knee and hip replacements, dental crowns, and skull implants [2,3]. When it comes to titanium alloys for use in biomedical applications, Ti6Al4V is thought to be the most advantageous [4–6]. Furthermore, Ti6Al4V alloy's extraordinary osseointegration rates, in slight strength-to-mass ratios, and its corrosion resistance have made it useful in orthopedic applications [7,8]. When choosing metallic materials for biological applications, the main considerations are mechanical performance, biocompatibility, tribological properties, and corrosion resistance [9]. To

 doi:10.20944/preprints202509.1018.v1

better comprehend biocompatibility and resistance to corrosion under physiological conditions, scientists have closely examined how it behaves in situations that closely resemble the aggressive characteristics of biological fluids. However, the effects of biomolecules on the characteristics of titanium and titanium alloys are poorly understood [10–14]. Several authors have demonstrated that Ti and its alloys corrode when subjected to various biocompatible fluids, including Ringer's solution, NaCl, and artificial saliva [15,16]. A surface oxide film may have an absorbent external layer and a dense inner layer, depending on the circumstances. The primary factors influencing titanium implant biocompatibility are the oxide layer's electrochemical properties and its long-term resilience in biological settings [17–22]. Proteins and amino acids, as biomolecules, can stick to metallic exteriors and function as ligands, forming metal complexes on the metal surface that might slow down corrosion processes [23]. There are numerous varieties of corrosion inhibitors, and each one functions differently and has a different chemical makeup. Despite being used as metal corrosion inhibitors, inorganic corrosion inhibitors like phosphates and chromates have several drawbacks, chief among them being their toxicity. Organic corrosion inhibitors containing heteroatoms of nitrogen, oxygen, and sulfur, conjugate π-bonds, and aromatic rings in a chemical construction exhibit notable inhibitory activity [24,25]. Metal corrosion is considerably reduced by the adsorption of corrosion inhibitor particles on the metallic surface. Their chemical and structural properties affect how well corrosion inhibitors work [26,27]. All of these corrosion inhibitors are hazardous, and their manufacture is expensive and difficult [28,29]. When these corrosion inhibitors are released into the soil and water, they build up and cause environmental problems. It is also necessary to add organic solvents to dissolve these inhibitors in the medium, which exacerbates the pollution problems in the environment.

Many medications, including antibiotics and other medications, effectively stop corrosion [30,31]. In this drug-based corrosion inhibitor, cyclic organic molecules with rings of five or six members are present. Nitrogen, sulfur, and oxygen are found in the basic five-membered heterocycles pyrrole, thiophene, and furan, respectively. The rings have six members, including pyridine, pyrimidine, and triazines. Pyrazoles, imidazoles, oxazoles, thiazoles, thiadiazoles, pyrazines, and pyrimidines are examples of corrosion-inhibiting compounds that can be made by substituting nitrogen or other elements for more than one carbon atom. It is important to keep in mind that these elementary constructions are insufficient to stop corrosion on their own. Thus, more heterocycles, phenyl rings, π-bonds, and useful groups must be added to these molecules to modify them further. Many drugs have gotten too much attention in recent years [32–36]. In comparison to the more conventional corrosion inhibitors based on heterocyclic molecules, this method of drug use is realistic, cost-effective, and time-efficient [37]. A muscle relaxant with analgesic and anti-inflammatory properties, thiocolchicoside (TCC) is the drug most frequently recommended to treat sudden, painful muscle spasms [38–40]. Easy solubility in water, low cost, non-toxicity, and the existence of seven-membered rings that facilitate adsorption are some of TCC's benefits as a safe corrosion inhibitor.

To our knowledge, no information has been published in the literature about thiocolchicoside's (TCC) ability to suppress corrosion of Ti6A14V alloy or any other metal.

This study thus documents, for the first time, the thiocolchicoside (TCC) inhibitory activity of Ti6A14V alloy in a saline solution (SS). The corrosion behavior of the Ti6A14V alloy in an SS is assessed in this work using EIS, OCP, and PPCs in combination with SEM/EDS, AFM, and CA probes. Moreover, the structural properties and adsorption performance of TCC were examined theoretically using density functional theory (DFT), natural bond orbital (NBO) analysis, and molecular dynamics simulation (MD) techniques to investigate their inhibition effectiveness. These findings lay the groundwork for a comprehensive understanding of Ti alloy corrosion in biomedical settings, with exceptional corrosion resistance for use in biomedical applications.

 doi:10.20944/preprints202509.1018.v1

2. Materials and Methods

Epoxy cold resin mounting of alloys was used to create the Ti6A14V electrode, exposing 1.0 cm^2 of the electrode surface to a saline solution (SS) (0.9% NaCl, pH 5.0). In electrochemical experiments, the Ti6A14V electrode served as the working electrode. Japan Coating Co., Ltd., Japan, supplied the samples. There are references to the Ti6Al4V alloy's chemical composition elsewhere [30]. Subsequently, electrode samples are routinely refined with sandpaper of several classes (500, 800, and 1200) and washed with distilled water and acetone. The electrodes are stimulated in 1.0 M hydrogen fluoride for 1 minute and then rinsed with double-distilled water. Platinum served as the auxiliary electrode. Ag/AgCl was utilized as a reference electrode for all potential measurements. Deionized water and analytical-grade reagents were used to produce an SS for each experiment. TCC is sourced from the Egyptian pharmacy (Figure 1). TCC concentrations were determined by dissolving five tablets (4 mg) in 100 milliliters of deionized water and using 0.9% NaCl. A Gamry Instrument Potentiostat/Galvanostat/ZRA, model number 1000, was utilized for the electrochemical analyses. The PPCs were performed at a sweep rate of 2 mVs^{-1}. The EIS figures were traced utilizing a wide range of frequencies (100,000 Hz to 10.0 mHz) and an amplitude of 5 mV peak to peak. The corrosion susceptibility of the micro-implant was determined by evaluating electrochemical experiments under the recognized test methodology. Every test was run in triplicate. Using a JEOL JEM-1200EX II type SEM, the surface morphology of the test samples was inspected. AFM and a WiTec Alpha 300R Raman Imaging Microscope together. With a silicon cantilever set to 280–300 kHz and a force constant of 42 N/m, the AFM pictures were captured in non-contact mode. The CA evaluation was accomplished utilizing the Model -DSA258 (KRUSS GmbH, Germany) to estimate the hydrophobicity of the metal surface.

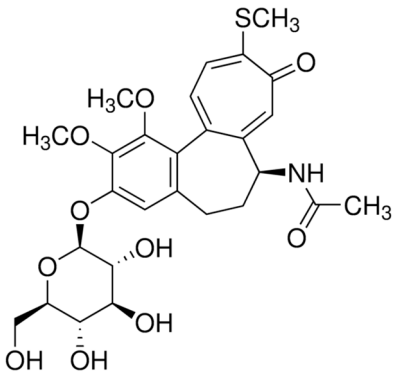

Figure 1. Chemical structure of thiocolchicoside (TCC), Chemical Formula C27-H33-N-O10-S, (MWt. 564).

2.1. Computational Studies

2.1.1. Quantum Theoretical Computations

Using Gaussian View 5.0.9 determined the various molecular parameters of TCC by visualizing the simulation of the structural features and the vibrational frequencies. Becke's theoretical calculations, which depend on DFT, are performed using Lee–Yang–Parr (B3LYP) three-parameter function with a 6–311++ G (d,p) basis set by using the Gaussian 09 program package [41]. The global reactivity determined by DFT which applied to, calculate the E_{HOMO} of the highest occupied energies, and lowest unoccupied molecular orbital E_{LUMO}, gap energy (ΔE), moment dipole (μ), ionization (I) energy, electron affinity (Y), absolute (ϕ) electronegativity, (ψ) absolute hardness, (S) absolute softness, global electrophilicity (ω), nucleophilicity (ε), power electro-accepting (ω+), power electro-donating ($\omega-$), the donation back ΔE, fraction transferred electrons (ΔN) and energy inhibitors interaction ($\Delta E_{TiAlV/TCC}$). Utilizing Fukui functions, which are used to analyze the local reactivity of the studied inhibitor molecules [42–44]. The orbital interactions, atomic charges, and their effects on

 doi:10.20944/preprints202509.1018.v1

the structure and stability of the examined structures were calculated using the natural bond orbital (NBO) approach.

2.1.2. Molecular Simulation Dynamics

The TCC inhibitor is adsorbed on the surface by Molecular Dynamics Simulation (MD). The TCC and the Ti6Al4V surface interaction were examined in an interacting system without any molecular solvent [45]. Dimensions with a simulation box of 24.32 Å × 24.32 Å × 9.10 Å were performed to model the descriptive part; periodic boundary conditions and the interface free of capricious boundary impacts were applied. Initially, the construction and relaxation of the Ti alloy surface with higher periodicity and surface area are used as a supercell. Finally, the Ti alloy surface has a thickness of 30 Å for a vacuum slab capable of learning the TCC that interacts with the Ti alloy surface. In the calculation used the non-bond cutoff structure's layers were used. The TCC inhibitor compound could interact with ten surface layers of Ti alloy atoms in non-bonding interactions without requiring excessive computation time. Afterwards, the structure was converted to 3D periodicity. The Dynamics Discover molecular module investigates thermodynamic parameters such as time simulation, temperature, and pressure, as well as the initiation of dynamic computation procedures for performing molecular dynamics simulations [46–48].

2.1.3. NBO Analysis

Natural Bond Orbital (NBO) analysis originated as a technique for studying hybridization and covalence effects in polyatomic wave functions that particularly exhibited hydrogen-bonded and other strongly bound van der Waals complexes [49]. The covalence effects in molecules are described by the filled NBOs σ of the ''natural Lewis's structure'' [50]. However, the non-covalent effects were described by the general transformation to NBOs that leads to orbitals that are unoccupied in the formal Lewis structure. The symbols σ and σ* are used in a generic sense to refer to occupied and unoccupied orbitals of the formal Lewis structure, though the former orbitals may be core orbital's (CR), lone pairs (LP), σ or π bonds (σ, π), and so forth, and the latter may be σ or π antibound (σ*, π*), or extra valence shell Rydberg (RY*) orbitals.

The NBO analysis reveals intra- and intermolecular interactions between donor and acceptor orbitals, specifically between filled (Lewis-type and bonding) and empty (non-Lewis or antibonding) natural bond orbitals. The stabilization energies of these interactions are estimated using second-order perturbation theory [49]. According to the equation below, the stabilization energy $E^{(2)}$ [50] associated with electron delocalization between the donor NBO (i) of electrons and the acceptor NBO (j) of electrons is calculated following equation (1):

$$E^{(2)} = \Delta Eij = qi\ (F\ (ij)\ 2\ /\varepsilon j - \varepsilon i), \quad (1)$$

Fijis (ij) is an element of the off-diagonal NBO Fock matrix, qi represents the occupation of the donor orbital, εi and εj are the energies of the diagonal elements of NBO orbitals of the acceptor and the donor, respectively.

3. Results and Discussion

3.1. TCC as an Efficient Inhibitor for Ti6Al4V Alloy

3.1.1. PPCs

The influence of TCC on the corrosion characteristics of the Ti-alloy in an SS was examined through the polarization technique. Figure 2 examines the Tafel PPCs of the Ti-alloy following a 1-hour immersion in an SS with different concentrations of TCC (40-200 mg/l) at 310 K. Potentiodynamic variables derived from Tafel plots contain corrosion potential (E_{corr}), corrosion current (I_{corr}), and cathodic and anodic Tafel slopes (βc and βa). Figure 2 and Table 1 show that the addition of TCC under investigation results in a reduction in both I_{corr} and the rate of corrosion (CR). This decreasing effect is enhanced by raising the TCC concentrations. For example, I_{corr} dropped from

 doi:10.20944/preprints202509.1018.v1

3.08 x10^{-6} A cm^{-2} (without TCC) to 2.32 x10^{-7} A cm^{-2} (with 200 mg/l of TCC). In addition, the CR was lowered by 13.5 times when 200 mg/l of the TCC inhibitor was present (Table 1).

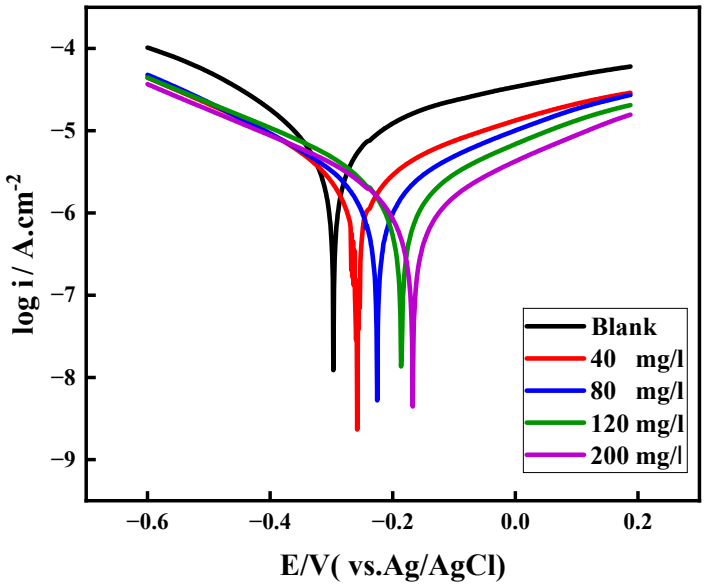

Figure 2. PPCs of Ti6Al4V alloy after immersion for 1 h in an SS in the absence and presence of different TCC concentrations, scan rate 2 mVs^{-1} at 310 K. .

Furthermore, when TCC concentration increased, the corrosion potential (E_{corr}) value demonstrated a discernible shift toward more noble potentials. TCC appears to be a mixed-type inhibitor that influences both anodic and cathodic polarization. The following relationship was used to calculate the inhibition effectiveness, η_{Pol} (%), from the measured I_{corr} values [47]:

$$\eta_{Pol}\ (\%) = \theta \times 100 = \frac{Icorr - Icorr(inh)}{Icorr} x100 \qquad (2)$$

While θ represents the surface covering, I_{corr} and I_{corr}(inh) stand for the corrosion current without and with varying TCC concentrations, respectively. Higher TCC concentrations lead to higher η_{pol}%. For instance, at a small amount of TCC (40 mg/l), the η_{Pol}% reaches 52.50%; however, at a higher concentration (200 mg/l), it achieves 92.40%. The results imply that TCC molecules are adsorbed at the interface between the Ti6Al4V alloy and the solution, creating an insulating film that shields the electrode surface and partially blocks the active sites of the corrodent. When the TCC concentration rises, more TCC molecules adsorb on the surface of the alloy, increasing its coverage. This is illustrated by the increase in η_{pol}% with higher inhibitor dosages. The surface coverage, for example, rises from 0.525 (at 40 mg/l of TCC) to 0.924 (at 200 mg/l). The TCC monolayer acts as an efficient protective film, suppressing both the oxidation and reduction processes, as demonstrated by the changes in (βa) and (βc) as the inhibitor's concentration increases.

Table 1. Tafel parameters obtained for a Ti6Al4V alloy in an SS with different concentrations of TCC at 310 K.

[TCC] mg/l	I_{Corr} A cm^{-2}	-E_{Corr} / V	β_a (V dec^{-1})	β_c (V dec^{-1})	CR Mpy	Θ	η_{Pol} (%)
0.0	3.08 x10^{-6}	0.297	0.210	0.294	0.396	-	-
40	1.46 x10^{-6}	0.255	0.656	0.238	0.188	0.525	52.50
80	9.10 x10^{-7}	0.226	0.128	0.108	0.117	0.704	70.40
120	5.51 x10^{-7}	0.189	0.077	0.067	0.070	0.821	82.10
200	2.32 x10^{-7}	0.170	0.035	0.050	0.029	0.924	92.40

 doi:10.20944/preprints202509.1018.v1

3.1.2. Impedance Analysis

EIS was employed to analyze the alterations in the protective barrier/SS interface that transpired when the Ti6Al4V alloy samples were exposed to an SS having different concentrations of TCC. A single, extremely polarization-resistant capacitive loop was observed in SS Nyquist plots (Figure 3a) with the addition of TCC. The increased number of adsorbed molecules on the surface of the Ti6Al4V alloy and the improved surface coverage of TCC on the Ti6Al4V alloy due to the adsorption process are the reasons why a study of the Nyquist drawing reveals that the circumference of the half-circle enhances when TCC is present.

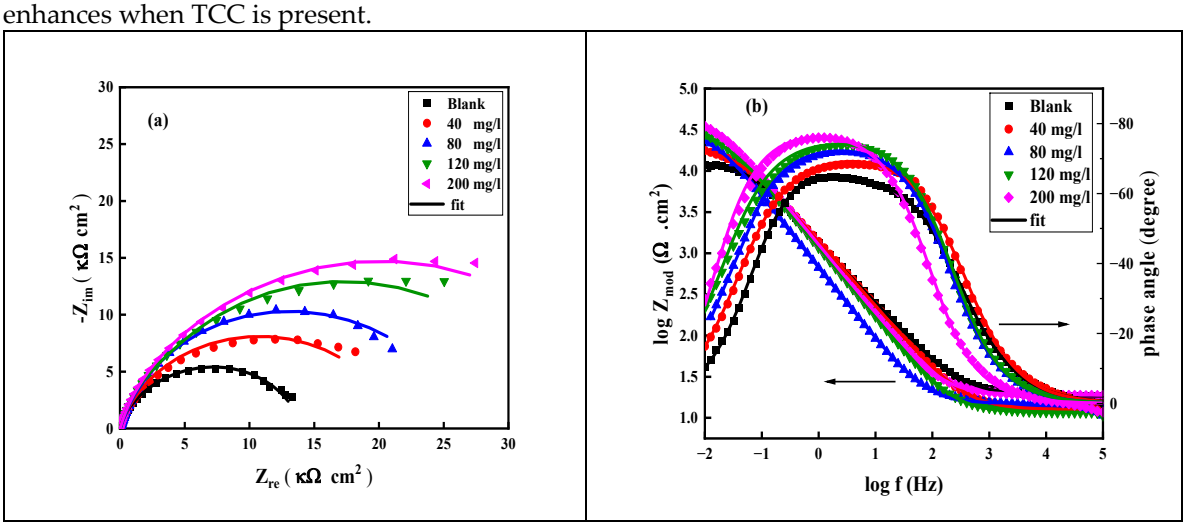

Figure 3. a) Nyquist plots and (b) Bode plots of EIS data of Ti6Al4V alloy in a SS at different TCC concentrations at 310 K.

Figure 3b depicts the impedance curves and corresponding phase angle versus frequency. The addition of the corrosion inhibitor increases the phase angle and the absolute impedance value. The adsorption and inhibition are supported by the increase in log |Z| values that occurs when the TCC inhibitor is introduced to the SS. These findings corroborate the enhanced capacitive functioning of the adsorbed TCC film at the interface between the Ti-alloy and SS [51,52]. This demonstrates how TCC is adsorbed and how the TCC-Ti alloy is shielded by the development of a protective layer. High protective effectiveness and a reduction in the TCC-Ti alloy's corrosion rate at higher frequencies are indicated by a shift in phase angle towards 90 degrees as TCC concentration rises [53,54]. The increased phase angle values for the inhibited samples demonstrated the protective layer of inhibitors covering the Ti-alloy surface. The increase in width and move to minimal frequencies of the single maximum in the Bode graphs lends support to the theory that inhibitor molecules form protective coatings [55,56].

As demonstrated in Figure 4, the obtained EIS data is fitted employing a two-time constant equivalent circuit (EC) [57]. The chi-square value ($\chi 2$) (Table 2) illustrates the discrepancy between the modeled data and the observed value of impedance analysis; a smaller chi-square value denotes less variance. The EC is composed of the constant phase elements (Q_f and Q_{dl}), which include the film capacitance (C_f) and double-layer capacitance (C_{dl}), the electrolyte resistance (Rs), the charge transfer resistance (R_{ct}), and the resistance of the film formed on the Ti-alloy surface (R_f) EC [58]:

 doi:10.20944/preprints202509.1018.v1

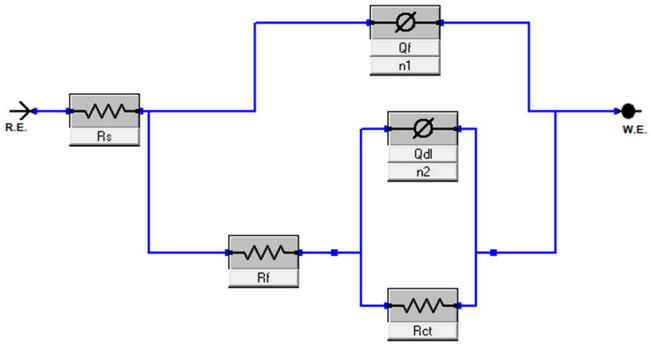

Figure 4. The equivalent circuit used for the EIS data fitting.

When an ideal capacitor is not suitable for the corroded Ti-alloy electrode, a constant phase element (CPE, Q) is employed to substitute capacitance C because of the heterogeneity of the Ti-alloy surface following corrosion in the medium. The following equation (3) defines the CPE impedance [58]:

$$Z_{CPE} = Q^{-1}(i\omega)^{-n} \quad (3)$$

The angular frequency $\omega = 2\pi f$, the CPE exponent, which has assessments extending from -1 to 1, and an imaginary number with i^2 equal to -1 are the parameters (i, ω, n) in that order. It is crucial to keep in mind that the arbitrary value of n has a specific relevance when characterizing the circuit elements identified by CPE. Additionally, the CPE and the double layer's capacity (C_{dl}) have the following relationship [59]:

$$Cdl = \sqrt[n]{Q.Rp^{1-n}} \quad (4)$$

Data on several electrochemical parameters, including phase shift (n), double-layer capacitance (C_{dl}), polarization resistance (R_P), solution resistance (R_S), and Q_{CPE} constant, are shown in Table 2. The Rp, which is the addition of R_f and R_{ct}, can be applied to assess a material's capability to resist corrosion in corrosive environments. The correlation between the corrosion rate and the Rp is inverse [59]. Table 2 shows the fitting data for the TCC inhibitor at different doses that were obtained from the EIS diagrams. As shown in this table, the Q_{dl} values of TCC and the blank system differ significantly. The drop in Q_{dl} is usually caused by the TCC molecules' propensity to stick to the Ti-alloy surface, emphasizing the role of molecular adsorption in preventing corrosion [60].

As a result, the lower Q_{dl} indicates the TCC protective film's superior barrier function. On the other hand, when TCC is present at 200 mg/l, the polarization resistance (R_P) rises from 7.85 kΩ cm^2 for the blank solution to 78.88 kΩ cm^2. This implies that the adsorbed TCC barrier layer on the electrode surface has thickened. TCC provides the best protection because it adsorbs on the Ti6Al4V alloy surface. The inhibitory efficiency in Table 2 is estimated and reported employing the following formula [61]:

$$\eta EIS\ (\%) = \frac{Rct - R°ct}{Rct} x100 \quad (5)$$

where R_{ct} and $R°_{ct}$ stand for charge transfer resistances in the presence and absence of TCC inhibitors, respectively. The electrochemical variables R_s and R_{ct}, which were determined using impedance fitting, and the estimated values Q_{dl} and ηEIS (%), are recorded in Table 2. The results demonstrate that the effectiveness of inhibition went up from 64.1 to 90.1% as the TCC concentration was increased from 40 to 200 mg/l. Table 2 shows that R_{ct} increases significantly as TCC concentration increases, while Q_{dl} decreases. A high R_{ct} indicates a slow-corroding system. Furthermore, enhanced inhibitor protection has been linked with a reduction in metal capacitance. The TCC functioned through adsorption at the Ti-alloy/SS interface, as evidenced by the reduction in Q_{dl} caused by a rise in the thickness of the electrical double layer and a decline in the limited dielectric constant.

 doi:10.20944/preprints202509.1018.v1

Table 2. Fitting parameters of EIS obtained for a Ti6Al4V alloy in an SS with different concentrations of TCC at 310 K.

Concentration mg/l	R_s (Ω cm^2)	R_{ct} (kΩ cm^2)	Q_{dl} (F cm^2 Hz^{1-n1})	R_f (KΩ cm^2)	Q_f (F cm^2 Hz^{1-n2})	R_p (R_f + R_{ct}) (kΩ cm^2)	$\chi 2$ x10^{-9}	Θ	η_{EIS} (%)
0.0	16.79	7.80	79.61x10^{-6}	0.045	197.0x10^{-6}	7.85	0.227	-	-
40	18.30	21.77	59.02x10^{-6}	0.067	182.9x10^{-6}	21.83	0.552	0.641	64.1
80	20.83	25.01	47.54x10^{-6}	0.073	166.2x10^{-6}	25.08	0.027	0.688	68.8
120	33.25	47.12	33.29x10^{-6}	0.088	140.3x10^{-6}	47.20	0.732	0.834	83.4
200	55.53	78.79	22.64x10^{-6}	0.096	77.60x10^{-6}	78.88	0.856	0.901	90.1

3.1.3. OCP Measurements

The effects of varying TCC inhibitor doses (40–200 mg/l) at 310 K on the OCP values of the Ti6Al4V alloy concerning dipping period in an SS are examined, with findings presented in Figure 5. For the development of barriers on the Ti6Al4V alloy surface, the corrosion potential progressively increased to more noble potential values before reaching steady-state potential values (after 300 s) at approximately, -0.354, -0.344, -0.328, -0.275, and -0.241V, which correspond to 0, 40, 80, 120, and 200 mg/l of TCC inhibitor concentration, respectively. The steady-state potentials produced indicated improved surface film stability. The potential shifts toward a more noble direction as TCC concentration in the SS goes up, enhancing the film thickness and further isolating the base metal from the SS. This characteristic accelerates the production of protective layers, which prevent Ti6Al4V alloys from disintegrating and reduce corrosion.

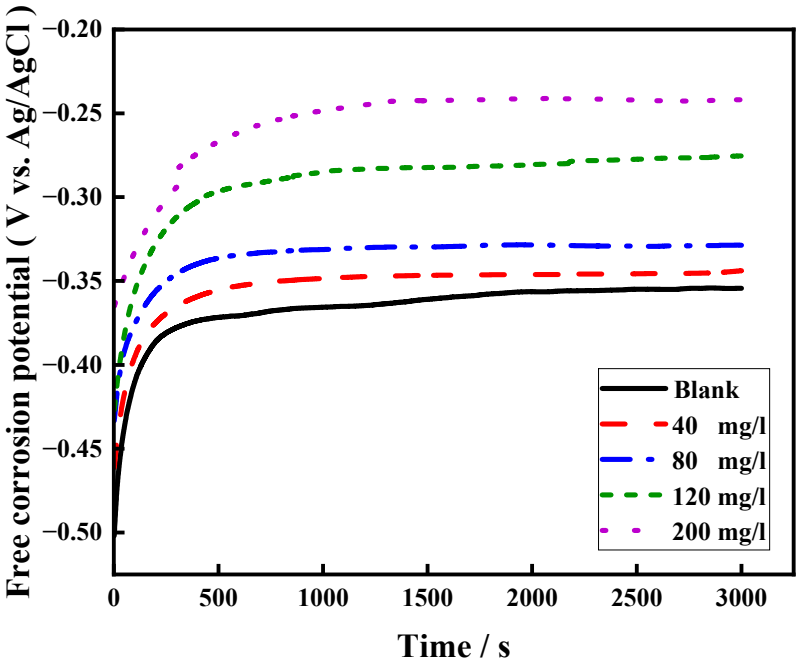

Figure 5. OCP behavior as a function of time for Ti6Al4V alloy in an SS at different concentrations of the TCC at 310 K.

 doi:10.20944/preprints202509.1018.v1

3.2. The Impact of Temperature and Thermodynamic Investigations

3.2.1. PPCs

PPCs measurements for the Ti6Al4V alloy under investigation in an SS, both with and without TCC, were tested at temperatures extending from 310 to 340 K to give detailed knowledge about the kind of inhibitor adsorption and its efficiency. Table 3 and Figure 6 (a, b) show that the temperature raised the I_{corr} and the CR regardless of the existence of TCC.

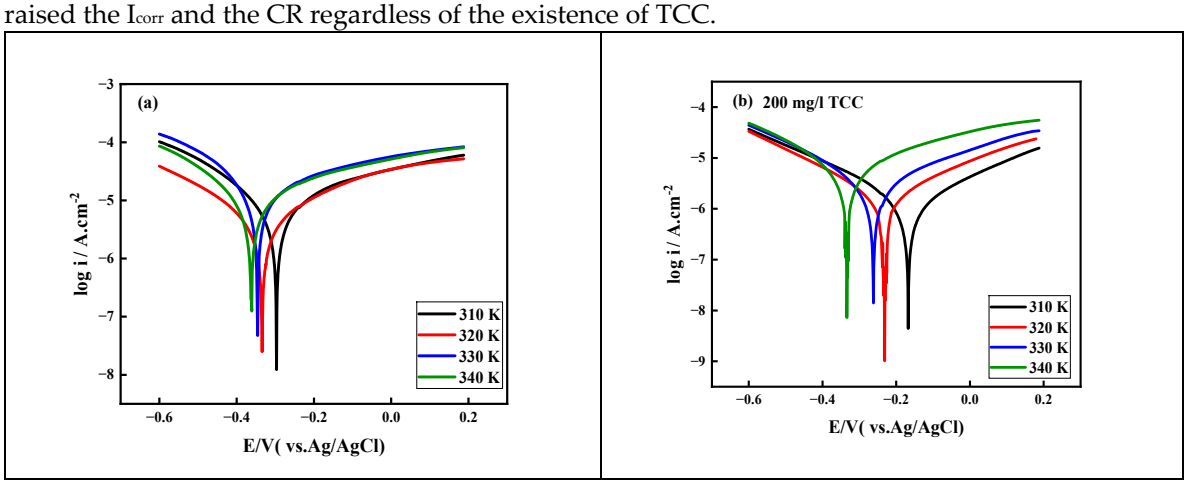

Figure 6. (a,b) PPCs of Ti6Al4V alloy electrodes in an SS recorded with a scan rate of 2 mVs^{-1} at different solution temperatures without and with 200 mg/l TCC.

In the absence of TCC, the E_{corr} values moved from - 0.297 V to -0.362 V as temperature increased from 310 to 340 K. On the other hand, the inclusion of the TCC in the SS moved the potential to more negative values (from -0.170 V to – 0.333 V). As the temperature increased, the E_{corr} values shifted to a higher cathodic potential.

These results also demonstrate that both the anodic and the cathodic reactions speed up as a result of increasing the temperature [62,63]. Therefore, as the temperature rises, corrosion visibly increases. The slopes of the βc and βa Tafel lines remain consistent as temperature increases. This reveals that whilst the corrosion mechanism is unaffected by temperature, the alloy surface begins to corrode. The findings showed that as the temperature rises, the inhibition efficiency descends. For instance, Table 3 illustrates the correlation between the TCC concentration and the Ti6Al4V alloy's efficiency of inhibition (η_{pol}%) at different temperatures. The observed behavior could be attributed to the inhibitor molecules being physically adsorbed, as higher temperatures may impair the adsorption process. As a result of the inhibitor adsorption and formation of a physical barrier on the alloy surface, a lowering in the alloy's reactivity in electrochemical processes occurs.

Table 3. Tafel kinetic parameters obtained for a Ti6Al4V alloy in an SS with and without the TCC at different solution temperatures.

Temperature K	I_{Corr} A cm^{-2}	$-E_{Corr}$ / V	β_a (V dec^{-1})	β_c (V dec^{-1})	Corr Rate mpy	Θ	η_{pol}%
0.00 mg/l							
310	$3.08x10^{-6}$	0.297	0.110	0.094	0.396	-	-
320	$5.29x10^{-6}$	0.334	0.313	0.262	0.681	-	-
330	$8.50x10^{-6}$	0.345	0.221	0.120	1.098	-	-
340	$1.22x10^{-5}$	0.362	0.425	0.238	1.574	-	-
200 mg/l							
310	$2.32 x10^{-7}$	0.170	0.035	0.050	0.029	0.924	92.4
320	$1.00 x10^{-6}$	0.223	0.144	0.154	0.084	0.825	82.5
330	$2.96x10^{-6}$	0.261	0.219	0.175	0.380	0.651	65.1
340	$7.09x10^{-6}$	0.333	0.518	0.314	0.913	0.418	41.8

 doi:10.20944/preprints202509.1018.v1

The Arrhenius equation (Eq. 6) and the transition state equation (Eq. 7) can be utilized properly to under- stand this phenomenon [64]:

$$\text{Log Icorr} = \frac{-\text{Ea}}{2.303\ \text{RT}} + \log \text{A} \qquad (6)$$

$$\text{Log}\frac{\text{Icorr}}{T} = \text{Log}\frac{\text{R}}{Nh} + \frac{\Delta Sa}{2.303R} - \frac{\Delta Ha}{2.303RT} \qquad (7)$$

Pre-exponential factor is denoted by A, Planck's constant (6.626176 x 10^{-34} Js) by h, Avogadro's number (6.022 x 10^{23} mol^{-1}), entropy and enthalpy of activation by ΔS_a and ΔH_a, and the corrosion process's activation energy by E_a. These equations are drawn as log I_{corr} and log (I_{corr}/T) versus the reciprocal of temperature, respectively, in Figure 7. The slopes and intercepts of these equations can be employed to assess the thermodynamic factors. The activation energy E_a and the constant A were calculated using the slope (-E_a/2.303R) and intercept (log A) of Eq. (6), respectively. The values of ΔH_a and ΔS_a were calculated using the slope (-ΔH_a / 2.303 R) and an intercept [(log (R/ Nh) + (ΔS_a / 2.303 R)] of Eq. (7), respectively. The assembled data is shown in Table 4. The TCC's adsorption on the surface of the Ti6Al4V alloy is essential to the protective mechanism. The TCC molecules may be adsorbed chemically or physically onto the Ti-alloy surface. E_a ranges from 40 to 80 kJ mol^{-1} for chemical adsorption and from 5.0 to 40 kJ mol^{-1} for physisorption. Because the E_a value is higher when TCC is present than when it is not, the results imply that the inclusion of the examined TCC decreases the dissolution rate of the Ti6Al4V alloy. Consequently, TCC may be a potent inhibitor in an SS to stop aggressive Ti6Al4V alloy corrosion. Considering that E_a is increased by the addition of TCC to the SS, and that the magnitude of the enhancement varies with the inhibitor concentration.

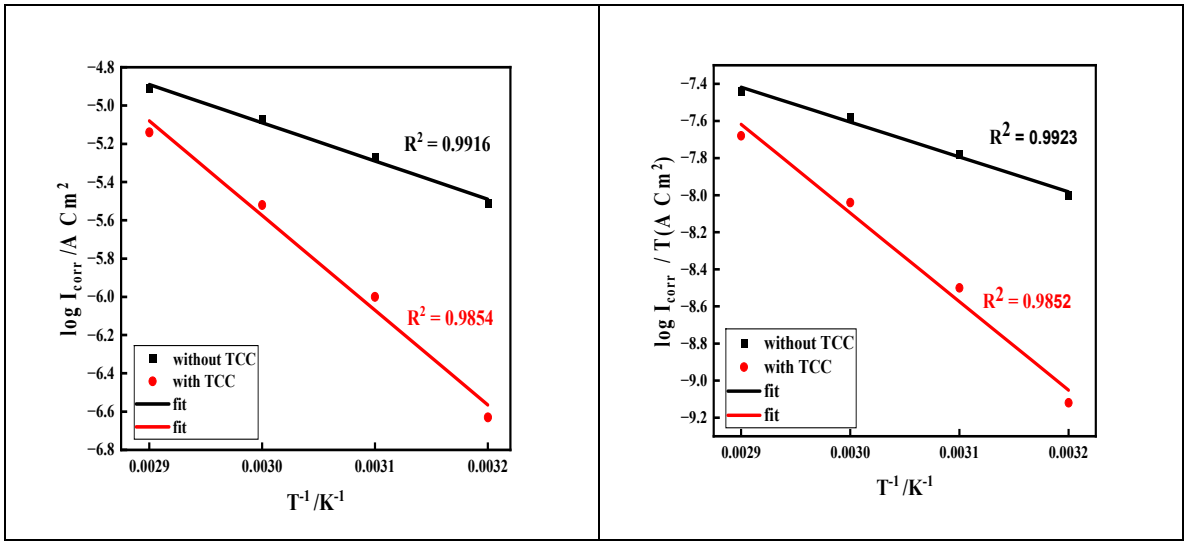

Figure 7. Arrhenius plot of log I_{corr} vs T^{-1}/ K^{-1} and transition state plot of log I_{corr}/ T vs T^{-1}/ K^{-1} with and without TCC.

The mechanism of adsorption on Ti6Al4V in an SS, including an inhibitor, was within the physical one (E_a = 35.79 kJ mol^{-1}) (Table 4). Positive ΔHa values indicate endothermic dissolution in Ti6Al4V alloy corrosion processes in aqueous solutions.

The higher values of ΔH_a in the inhibited (200 mg/l TCC) solution are caused by the strong corrosion-inhibiting activity. Furthermore, Figure 7 illustrates the correlation between log Icorr / T versus T^{-1}/K^{-1}, which is used to determine the values of ΔH_a and ΔS_a. The fact that the value of ΔH_a for TCC is more than that in the absence of TCC indicates that the corrosion rate of the Ti6Al4V alloy in an SS has decreased [65]. The activation entropy ΔS_a is negative and high with and without TCC (Table 4). Disorder decreases as one moves from reactants to activated complexes. This suggests the activated complex in the rate-determining step is an association step, not a dissociation step [65]. The low positive value of ΔH_a and the decline in inhibitory efficiency with temperature in the current investigation serve as evidence of physisorption. The apparent activation energy of the corrosion is higher in the presence of TCC (35.79 kJ mol^{-1}) than in its absence (14.46 kJ mol^{-1}).

 doi:10.20944/preprints202509.1018.v1

Table 4. Thermodynamic parameters in the presence and absence of TCC in an SS.

Solution	ΔHa (kJ mol^{-1})	ΔSa (J mol^{-1} K^{-1})	Ea (kJ mol^{-1})
Without TCC	13.59	-64.57	14.46
With 200 mg/l TCC	34.56	-33.62	35.79

3.2.2. Impedance Analysis

At different temperatures (310, 320, 330, and 340 K), EIS measurements are carried out in an SS both with and without TCC. Figure 8(a, b) uses the Nyquist plots to illustrate a single capacitive loop with a high polarization resistance. The Nyquist figure illustrates how the semicircle diameter decreases when TCC desorbs from the Ti6Al4V surface at high temperatures. As seen in Table 5, adding TCC to an SS at any given temperature raises the R_{ct} value compared to the solution without TCC at that temperature. The decrease in R_{ct} values of TCC with rising temperature indicates that the desorption of TCC from the Ti6Al4V surface leads to lower surface coverage of TCC on Ti6Al4V, higher corrosion rate, and subsequently decreased inhibitory efficiency.

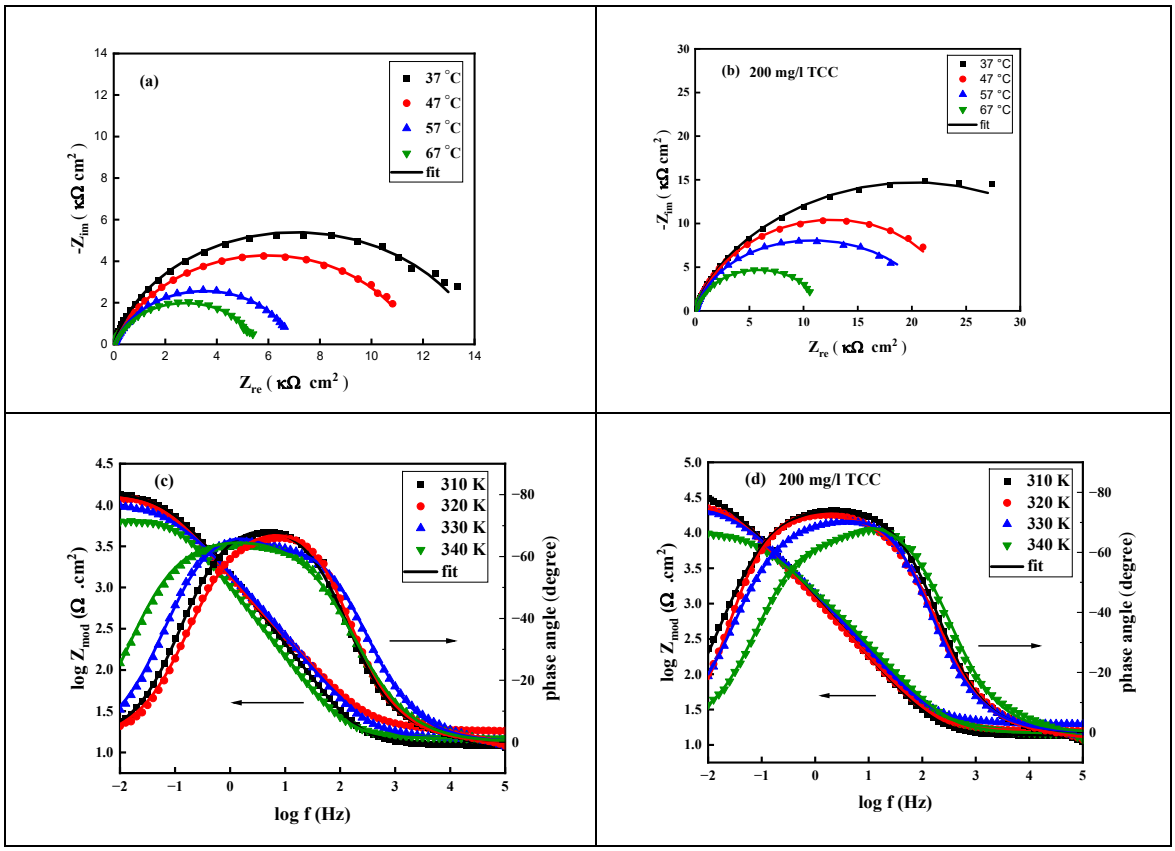

Figure 8. (a, b) Nyquist plots and (c, d) Bode plots of EIS data of Ti6Al4V alloy in an SS without and with 200 mg/l TCC, respectively, at different temperatures.

Table 5. Fitting parameters of EIS obtained for a Ti6Al4V alloy in an SS with and without TCC at different temperatures.

Temperature K	R_s (Ω cm^2)	R_{ct} (kΩ cm^2)	CPE_{dl} (F cm^2 Hz^{1-n1})	n	Θ	η_{EIS} (%)
0.00 mg/l						
310	16.79	7.80	79.61x10^{-6}	0.843	-	-
320	22.36	6.12	123.80x10^{-6}	0.829	-	-
330	44.19	5.43	235.11x10^{-6}	0.788	-	-
340	76.15	4.49	310.74x10^{-6}	0.769	-	-
200 mg/l						

 doi:10.20944/preprints202509.1018.v1

310	55.53	78.79	22.64×10^{-6}	0.855	0.901	90.10
320	23.14	32.15	57.20×10^{-6}	0.812	0.809	80.90
330	75.04	15.90	75.42×10^{-6}	0.755	0.658	65.80
340	14.06	7.57	94.12×10^{-6}	0.787	0.406	40.60

3.3. Adsorption Isotherm

The adsorption of TCC molecules at the Ti6Al4V/SS interface is explained by the following equation, which shows how organic molecules (TCC) replace water molecules:

$$TCC_{sol} + nH_2O_{ads} \leftrightarrow TCC_{ads} + nH_2O_{sol} \quad (8)$$

where n represents the number of water molecules that have been replaced, and TCC_{sol} and TCC_{ads} are the TCC compounds in the solution (liquid phase) and adsorbed on TCC-Ti6Al4V (adsorption phase), respectively [66]. The main factor influencing an organic compound's capacity to reduce corrosion is its capacity to adsorb onto the TCC-Ti6Al4V surface.

Knowledge of the mode of adsorption was necessary to comprehend the way of interaction between the TCC molecules and the surface of the alloy. Several adsorption isotherms were employed to analyze the investigated TCC's adsorption behavior. The Langmuir adsorption isotherm greatly matched the adsorption behavior of TCC at the Ti6Al4V/solution interface. Plotting C_{inh}/θ against C_{inh} using data generated from both polarization and EIS approaches yields straight lines with R^2 values of 0.9924 (Figure 9). Based on the Langmuir adsorption isotherm, which is described as [67]:

$$C_{inh} / \theta = 1/K_{ads} + C_{inh} \quad (9)$$

where C_{inh} is the TCC concentration, K_{ads} is the adsorption equilibrium constant, and θ is the amount of surface coverage (θ = (η (%) /100). Conversely, the standard adsorption-free energy, or ΔG^o_{ads} at 310 K, was estimated using the following formula [67]:

$$\Delta G^o_{ads} = - RT \ln (55.5\ K_{ads}) \quad (10)$$

Where 55.5 is the molar concentration of water, R is the universal gas constant, and T is the Kelvin temperature. Physisorption is known to work well with ΔG^o_{ads} that have values of -20 kJ mol^{-1} or lower, but chemisorption is necessary for those that have values greater than - 40 kJ mol^{-1} [68]. The ΔG^o_{ads} value was used to represent the adsorption type. Using the polarization and impedance results, the TCC's calculated ΔG^o_{ads} value is - 49.02 kJ mol^{-1} and - 49.20kJ mol^{-1}, respectively. A negative ΔG^o_{ads} value points to TCC adsorption on the Ti6Al4V surface occurring spontaneously (Table 6), suggesting that physisorption is the primary mechanism of TCC adsorption on the Ti6Al4V surface. Based on polarization and impedance measurements, the equilibrium constant's (K_{ads}) value may be calculated and found to be 10.87×10^4 and 11.50×10^4, respectively. The capacity of the adsorption forces among the TCC molecule and the alloy surface can be ascertained using the K_{ads} value. The greater K_{ads} value demonstrated the inhibitor's superior adsorption capacity onto the Ti6Al4V surface.

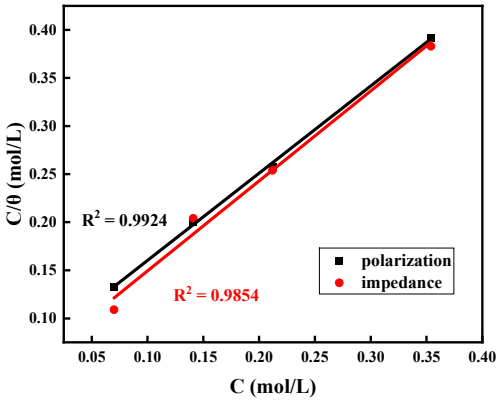

Figure 9. Curve matching of the polarization and impedance data acquired for Ti6Al4V alloys in an SS containing different TCC concentrations at 310 K, to the Langmuir adsorption isotherm.

 doi:10.20944/preprints202509.1018.v1

Table 6. The equilibrium constant of the inhibitor (K_{ads}), the standard free energy of adsorption (ΔG^{o}_{ads}) for Ti6Al4V alloys in an SS containing 200 mg/l TCC concentrations at 310 K, deduced by utilizing the Langmuir adsorption isotherm from the polarization and impedance data.

Alloy	K_{ads} (L mol^{-1})		ΔG^{o}_{ads} (kJ mol^{-1})	
	Polarization	Impedance	Polarization	Impedance
Ti6Al4V	10.87 x 10^4	11.50 x 10^4	-49.02	-49.20

3.4. Surface Morphology

To verify the mechanism of Ti6Al4V alloy degradation after corrosion in an SS, the electrode was investigated under a scanning electron microscope. Figure 10 displays the morphology of the surface of a polished Ti6Al4V alloy sample (Figure 10a) and the Ti6Al4V samples following a 24-hour immersion in SS with and without a TCC inhibitor (Figure 10 b, c). The barrier effect of alloy corrosion products in a given environment is determined by the characteristics and features of the resultant layer. The properties of thickness, homogeneity, compactness, porosity, solubility, fragility, and adhesion will influence the attack morphology and the corrosion rate of the underlying metal. As displayed in Figure 10 b, the Ti alloy submerged in SS experiences surface degradation in the SS solution. However, the micrographs demonstrate that when TCC is present, it forms a superior protective film that covers the entire alloy surface and protects it from deterioration (Figure 10c). This indicates that the inhibitory efficiency of the TCC is superior. The EDS measurements on the polished surface (Figure 10d) and for the alloy surface with and without inhibitor molecules (Figure 10e, f) show that the sample immersed in TCC contains N elements. This is an additional indication that the shielding layer is created by the TCC's adsorption on the alloy surface.

The UV spectra of TCC were measured both before and after the corrosion investigation to confirm the TCC inhibitor adsorption on the Ti alloy surface (Figure 11). The corrosive media in which the Ti6Al4V sample was not immersed had a higher absorbance, as indicated by the UV spectra, than the setting where the sample was dipped for a whole day. When the Ti6Al4V sample was immersed, some of the molecules from the TCC solution were adsorbed onto the surface. This implies that TCC has significant corrosion inhibition efficiency because it adsorbs on the Ti alloy sample effectively.

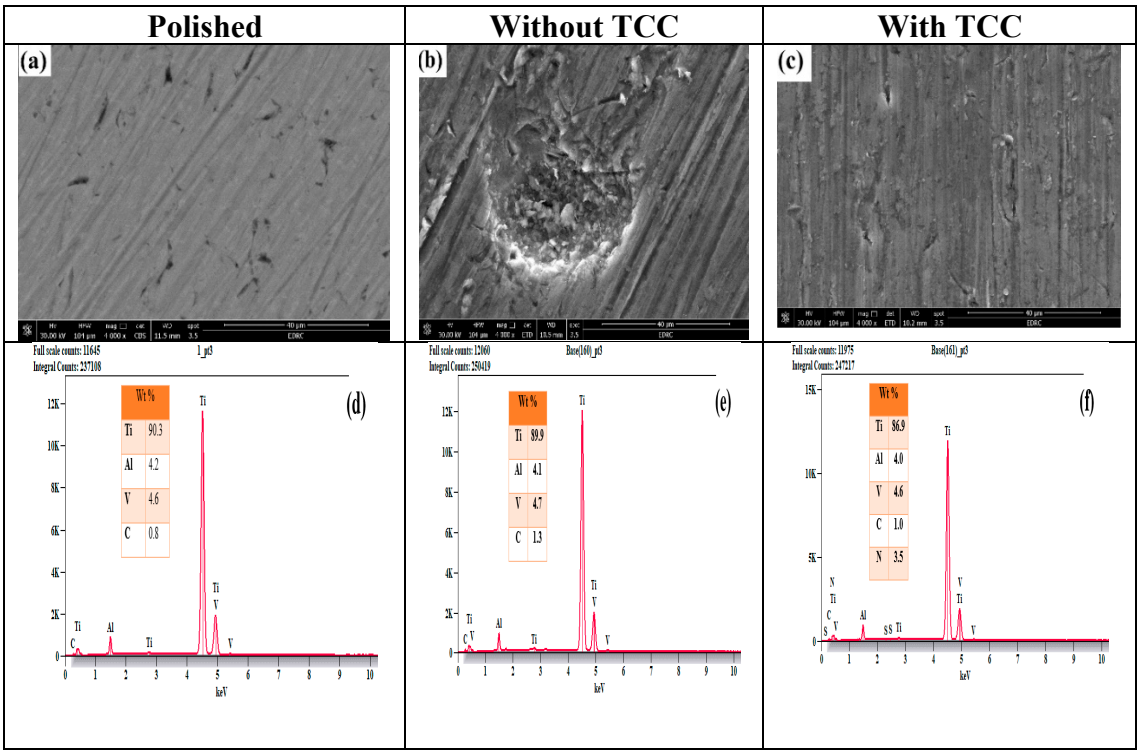

Figure 10. Surface morphology and EDS of Ti6Al4V alloy after immersion in SS (24 hours): (a) (d) polished sample, (b) (e) without TCC, and (c) (f) with TCC.

 doi:10.20944/preprints202509.1018.v1

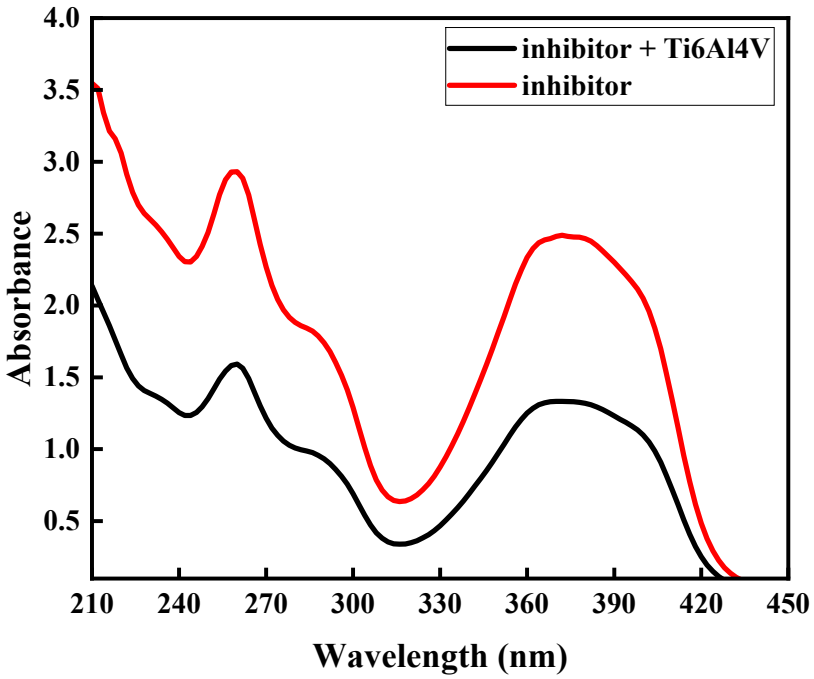

Figure 11. UV Spectra of TCC before and after the Ti6Al4V alloy immersion for 24 h.

3.5. Contact Angle (CA) Approach

Contact angle evaluations were made to confirm that a shielding cover of the TCC layer had formed on the Ti6Al4V alloy. A 4.0 µL drop of water was applied to the alloy surface to take this measurement. The images showing the CA evaluations for the Ti-alloy polished substrate (Figure 12a) and for the submerged Ti-alloy in SS without (Figure 12 b) and with TCC inhibitor (Figure 12c) are explored. When the polished alloy sample (Figure 12a) was dipped in the SS, its CA dropped from 68.8◦ to 32.8◦ (Figure 12b). This decrease suggests that the SS's corrosive activity has increased the surface's wettability. On the other hand, the contact angle of the alloy dipped in the TCC rose to 90.3◦ ° (Figure 12c). The adsorption of TCC on the Ti6Al4V alloy surface is shown by this notable increase in the CA, which suggests a decline in wettability and a rise in hydrophobicity. The formation of a hydrophobic shielding layer on the Ti alloy substrate successfully reduces the surface's interface with water, as confirmed by the increase in CA upon the introduction of the TCC. By acting as a safeguard and preventing the damaging environment from destroying the SS superficial. This protective coating confirms that the TCC inhibitor is effective in preventing degradation.

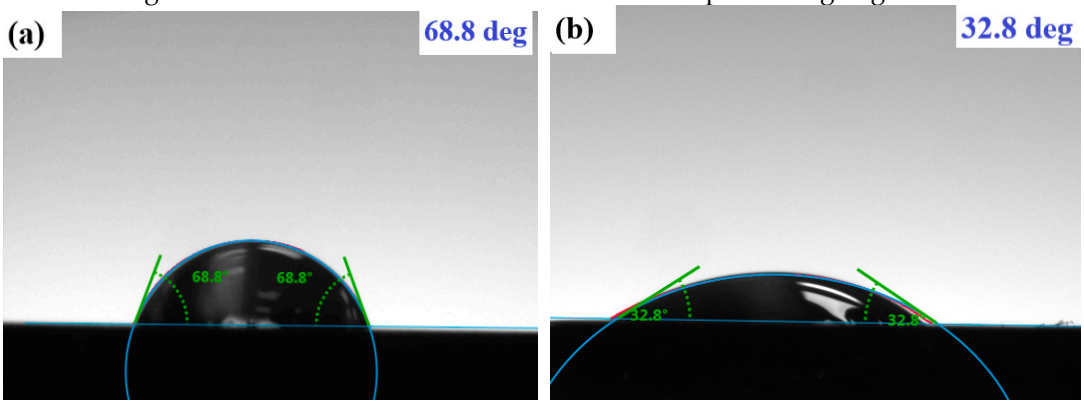

 doi:10.20944/preprints202509.1018.v1

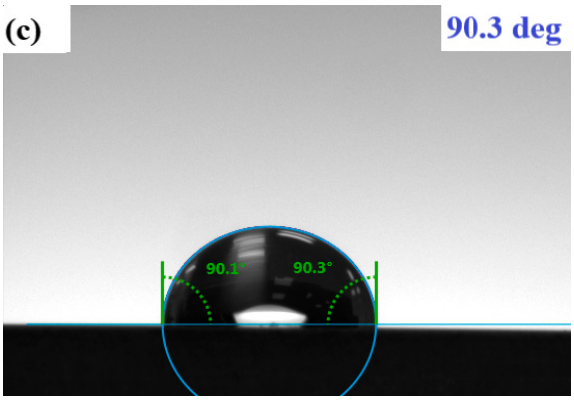

Figure 12. Contact angle values and images of a) polished Ti6Al4V surface; b) after immersion in SS for 24 h (blank); c) after immersion in SS and the presence of 200 mg/l TCC for 24 h.

3.6. Atomic Force Microscopy (AFM)

AFM is widely used to examine metal external morphology at the micro- and nano-scale levels in research examining the efficacy of corrosion inhibitors. The average surface roughness (Ra) evaluations of the Ti6Al4V alloy for the inhibited and uninhibited circumstances are carried out before and after a 24-hour immersion in SS. For comparison, the Ra for the polished sample is explored as shown in Figure 13a.The data unequivocally demonstrate that adding the TCC inhibitor causes a considerable drop in the Ra values for Ti6Al4V alloy in aqueous SS, and that this drop increases with increasing TCC dosages. By extending coverage on the alloy's surface and reducing the solution's corrosive effect, the TCC particles create protective layers, which is the cause of the observed phenomena. The three-dimensional AFM images of a very glossy Ti6Al4V alloy surface with a Ra value of 116 nm are explained in Figure 13a. The Ti6Al4V alloy surface is shown in Figure 13b and c before and after a 24-hour immersion at 37 °C in an aqueous SS, with Ra values of 289 nm and 347 nm, respectively, with and without TCC molecules. When contrasted to the exterior morphology in aqueous SS without the TCC, these images demonstrate that the exterior morphology of the Ti6Al4V alloy, as measured by height sensors, stays remarkably smooth even when TCC is present. Its capacity to protect the Ti6Al4V alloy surface from erosion in the damaging SS environment is demonstrated by this smoothness, which shows how well TCC inhibits. The outcomes, which show a notable reduction in surface roughness and enhanced surface protection, validate the inhibitor efficacy of TCC.

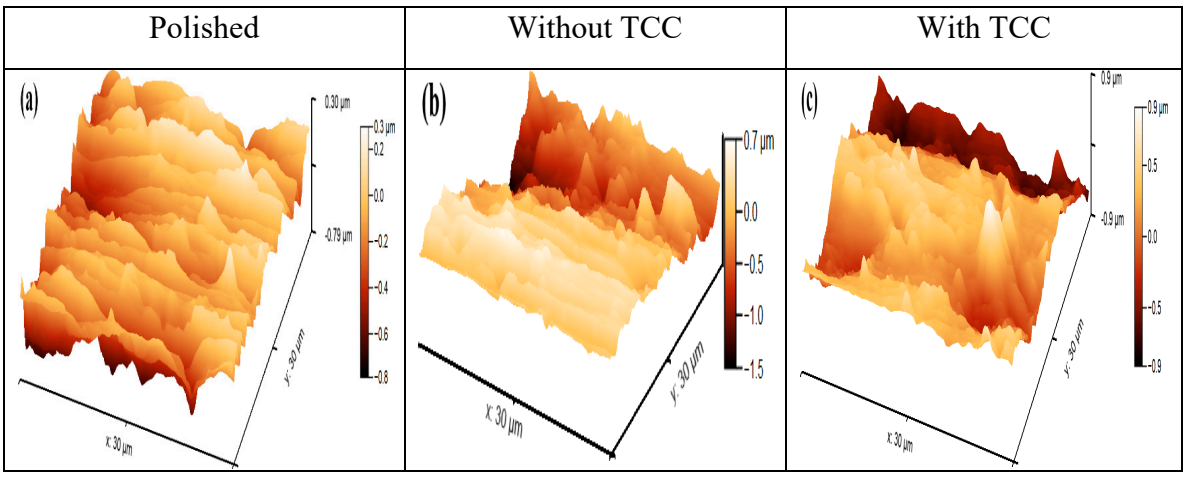

 doi:10.20944/preprints202509.1018.v1

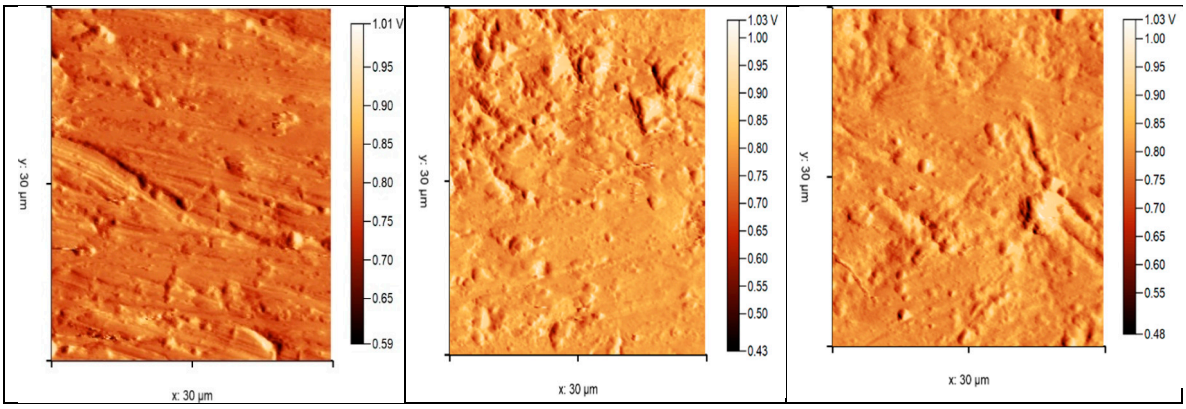

Figure 13. AFM images of Ti6Al4V alloy superficial: a) Polished Ti6Al4V alloy; b) Ti6Al4V alloy immersed in SS; c) immersed in SS in the presence of 200 mg/l TCC at 310 K.

3.7. DFT Approach

The recital of TCC as a corrosion inhibitor for Ti6Al4V alloy in artificial seawater (ASS) is further elucidated in Table 7, which summarizes the computed quantum chemical descriptors. Figures 14 and 15 show the customized molecular structure of TCC, as well as its Frontier Molecular Orbitals (HOMO and LUMO). The HOMO orbitals were primarily concentrated on the ring structures and heteroatoms of the TCC molecule, indicating that these regions are good targets for electrophilic attack at the metal interface. This electronic configuration enhances the molecule's inhibition efficiency, supporting the hypothesis that TCC can adsorb effectively onto the alloy surface, in alignment with the experimental findings. Furthermore, the energy gap ($\Delta E = E_{LUMO} - E_{HOMO}$) plays a critical role in this adsorption process and is considered a key factor affecting the inhibitory performance of the molecule's [41,48].

Table 7 presents the electrophilicity index (ω) and nucleophilicity index (ε) for both the neutral and protonated forms of the TCC inhibitor. In this study, the relatively low ω value indicates that TCC functions effectively as a nucleophilic corrosion inhibitor. The electron-accepting and electron-donating capabilities of the inhibitor are described by the electron-accepting power (ω^+) and electron-donating power (ω^-), respectively. A low ω^+ value suggests a strong electron-donating ability, while a higher ω^+ value implies enhanced charge-accepting capacity.

The interaction between TCC and the electrode surface is further characterized by the back-donation energy (ΔE), which reflects the stabilization gained from charge transfer during the adsorption. A negative ΔE value supports the occurrence of back-donation, contributing to increased inhibition efficiency. Specifically, Table 7 reports ΔE values of −0.272 eV for neutral TCC and −0.047 eV for its protonated form, $TCCH^+$. Additionally, the fraction of electrons transferred (ΔN) between the inhibitor and the alloy surface is presented in Table 7. The data display that when ΔN is lower than 3.6, the inhibitors can donate electrons to the Ti-alloy, which enhances their protective behavior. The interaction energy (ΔE) between the Ti6Al4V alloy surface and the TCC is a critical factor in evaluating the inhibitor's effectiveness. As shown in Table 7, the interaction energy for the neutral TCC molecule is 0.593 eV, while for the protonated form, it significantly increases to 216.352 eV, indicating a stronger adsorption tendency and, consequently, improved corrosion inhibition performance. The electron-donating capacity of the tested inhibitor was evaluated based on the fraction of electrons transferred (ΔN) to the metal surface. Additionally, the local reactivity of the TCC molecule was assessed using Fukui function calculations, providing further insight into its reactive sites and interaction potential with the alloy surface TCC [43,44].

The best sites for nucleophilic and electrophilic strikes in TCC molecules were determined by Fukui indices. The electrophilic attack is preferred when f^-_k has the maximum value and $\Delta f_k < 0$, while the f^+_k value is maximum and $\Delta f_k > 0$, the area in the molecule is liable to nucleophilic attack [42,46]. The Fukui indices for both the neutral and protonated forms of TCC and $TCCH^+$ are recorded in Table

 doi:10.20944/preprints202509.1018.v1

8. Notably, the inhibitor contains high-value sites that preferentially transfer electrons to the alloy's unoccupied orbitals.

The highest f^{+}_{k} and Δf_k values are S4, C6, N7, O8, C10, and O11 atoms in TCC, indicating that ideal sites for nucleophilic attack. In contrast, the most negative value of Δf_k and the largest value of f^{-}_{k} at N2, S15, O24, O25, and N30 in TCC show that these sites are more frequently attacked by electrophiles. Additional active sites are developed upon protonation, resulting in a significant alteration of the active sites present in the neutral molecule. For protonated molecules, the preferred sites for nucleophilic attack are S4, C6, and O8 in $TCCH^{+}$, presented in Table 8. Finally, the negative atomic charge values after protonation are slightly reduced from the TCC inhibitor's potential interaction sites on the surface [69].

The electrostatic potential (ESP) and molecular electrostatic potential (MEP) maps of the neutral TCC molecule are shown in Figure 16. The electron density is orderly in the following order: red > orange > yellow > green > blue [70,71]. The potential surrounding the rings is positive in our study. In contrast, the potentials are negative, which are around heteroatoms such as nitrogen, sulfur, and oxygen, implying the essential site for electrophilic attack.

Table 7. Computed quantum chemical descriptors for the studied neutral TCC and protonated $TCCH^{+}$ inhibitor in the gas phase.

Descriptors	Equations	TCC	TCC H^{+}
Energy of highest occupied molecular orbital (E_{HOMO}), (eV)		-4.291	-3.981
Energy of lowest unoccupied molecular orbital (E_{LUMO}), (eV)		-2.112	-3.601
Energy Gap ΔE	(LUMO-HOMO)	2.179	0.380
Dipole moment, (μ), (Debye)		1.983	19.758
Ionization energy (I) (ev)	$I = -E_{HOMO}$	4.291	3.981
Electron affinity (Y) (ev)	$Y = -E_{LUMO}$	2.112	3.601
Electronegativity (ϕ)	$\phi = \frac{I+Y}{2}$	3.201	3.791
Global hardness ψ	$\psi = \frac{I-Y}{2}$	1.089	0.190
Global softness (S)	$s = \frac{1}{\psi}$	0.918	5.263
Global electrophilicity (ω)	$\omega = \phi^2/2\psi$	4.705	37.820
Global nucleophilicity (ε)	$\varepsilon = \frac{1}{\omega}$	0.212	0.026
Electroaccepting (ω+) power	$\omega^{+} = \frac{(I+3A)^2}{16(I-A)}$	3.239	35.948
Electrodonating (ω^{-}) power	$\omega^{-} = \frac{(A+3I)^2}{16(I-A)}$	6.441	39.739
Net electrophilicity ($\Delta\omega\pm = \omega+ + \omega-$)	($\Delta\omega\pm = \omega+ + \omega-$)	9.680	75.687
Fraction of transferred electrons (ΔN)	$\Delta N = \frac{\phi_{Ti}-\phi_{inh}}{2(\psi_{Ti}+\psi_{inh})}$	-0.087	-0.108
Back-donation energy ΔE back-donation (ev)	$\Delta E_{back-donation} = -\frac{\psi}{4}$	-0.272	-0.047
Metal/inhibitor interaction energy $\Delta E_{Ti6Al4V/inhibitor}$ (ev)	$\Delta E_{\text{▭▭▭▭▭/▭▭▭▭▭▭▭▭}} = \frac{(\chi_{Ti}-\chi_{inh})^2}{4(\eta_{Ti}+\eta_{inh})}$	0.593	216.352

Preprints.org (www.preprints.org) | NOT PEER-REVIEWED | Posted: 12 September 2025 doi:10.20944/preprints202509.1018.v1

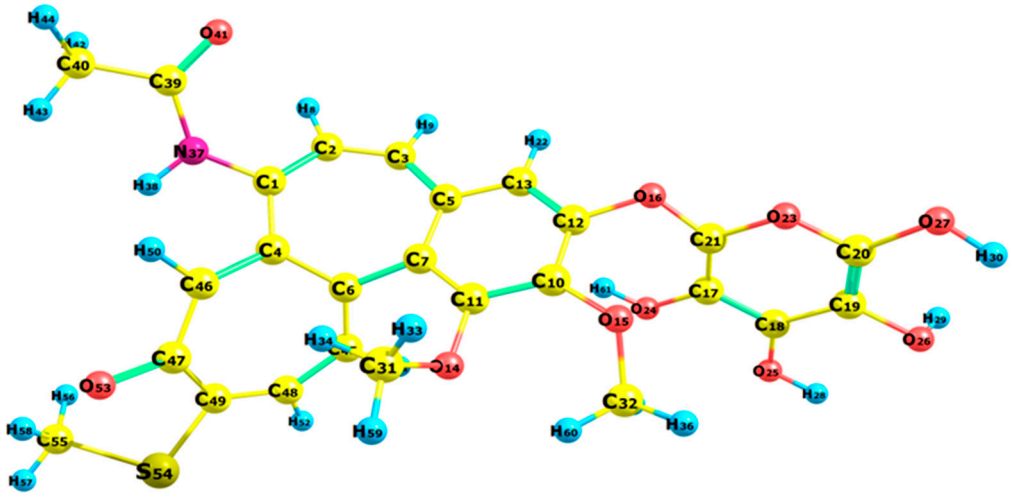

Figure 14. Optimized structure of the TCC using the B3LYP/6-311++G(d,p) basis set**.**

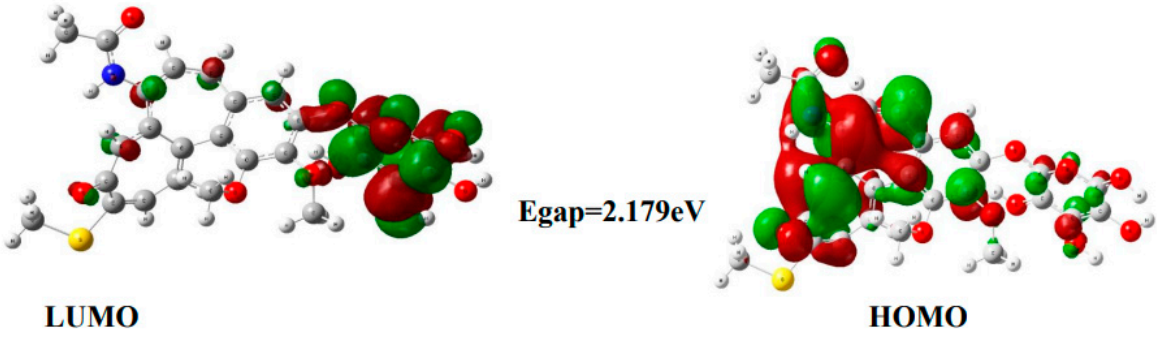

Figure 15. Frontier molecular orbitals HOMO and LUMO of the TCC using the B3LYP/6-311++G(d,p) basis set.

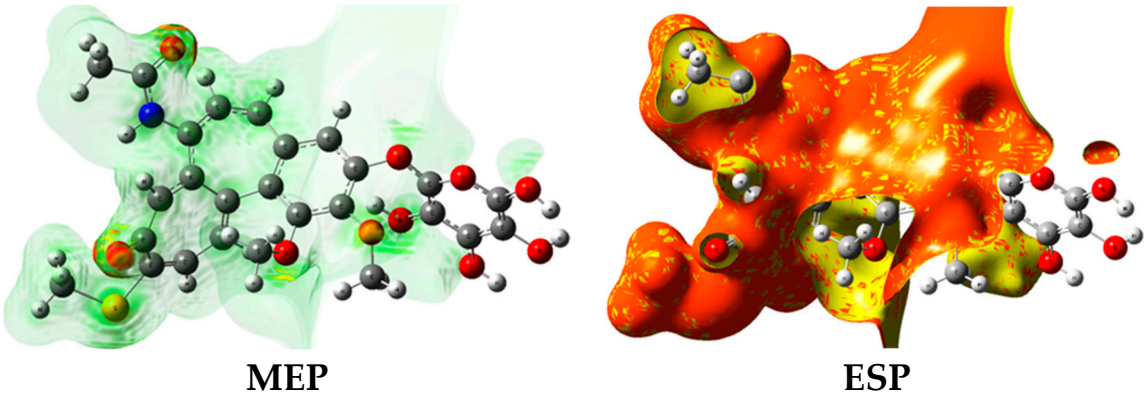

Figure 16. ESP and MEP distribution of the neutral TCC using the B3LYP/6-311++G(d,p) basis set.

Table 8. Fukui indices of the studied TCC.

Atom	$f(+)$	$f(-)$	Δf_k	Mulliken atomic charges
C(1)	0.008	0.010	0.002	-0.091
N(2)	0.046	0.040	0.006	-0.115
C(3)	-0.019	-0.021	0.002	0.013

 doi:10.20944/preprints202509.1018.v1

S(4)	**0.101**	**0.360**	**0.259**	**-0.144**
C(5)	**-0.020**	**-0.022**	**0.002**	**-0.091**
C(6)	**0.111**	**-0.004**	**0.107**	**-0.022**
N(7)	**0.129**	**0.032**	**0.097**	**0.275**
O(8)	**0.047**	**-0.004**	**0.043**	**-0.035**
C(9)	**-0.036**	**-0.012**	**0.024**	**-0.338**
C(10)	**0.042**	**0.000**	**0.042**	**0.469**
O(11)	**0.081**	**0.001**	**0.080**	**-0.355**
N(12)	**0.021**	**0.005**	**0.016**	**0.404**
N(13)	**0.009**	**0.003**	**0.006**	**-0.136**
C(14)	**-0.002**	**-0.004**	**0.002**	**-0.479**
S(15)	**-0.008**	**0.023**	**0.015**	**-0.373**
C(16)	**-0.001**	**-0.006**	**0.005**	**0.042**
C(17)	**0.008**	**0.020**	**0.012**	**-0.203**
C(18)	**-0.001**	**-0.004**	**0.003**	**-0.192**
C(19)	**0.005**	**0.002**	**0.003**	**-0.075**
O(20)	**0.022**	**0.008**	**0.014**	**-0.192**
C(21)	**-0.018**	**-0.005**	**0.013**	**0.309**
H(22)	**0.024**	**0.017**	**0.007**	**-0.39**
C(23)	**-0.004**	**0.009**	**0.005**	**0.308**
O(24)	**0.011**	**0.047**	**0.036**	**-0.448**
O(25)	**0.009**	**0.043**	**0.034**	**-0.448**
C(26)	**0.002**	**0.000**	**0.002**	**-0.192**
O(27)	**0.001**	**0.002**	**0.001**	**-0.075**
C(28)	**0.005**	**0.000**	**0.005**	**-0.192**
O(29)	**0.009**	**0.002**	**0.007**	**0.309**
N(30)	**0.013**	**0.060**	**0.047**	**-0.39**

3.7.1. Natural Bond Orbital (NBO) Analysis

Natural Bond Orbital (NBO) analysis provides insights into charge transfer within a molecule and its influence on molecular stability, particularly through the evaluation of atomic interactions. The second-order interaction energy (E^2) helps identify electron delocalization from filled orbitals—either bonding (BD) or lone pairs (LP)—to empty anti-bonding orbitals (BD*), thereby contributing to molecular stabilization, NBO [72]. In NBO terminology, BD refers to bonding orbitals formed between atoms, LP indicates lone pairs localized on individual atoms, and RY (Rydberg) represents orbitals with the highest principal quantum number and energy level, typically weakly bound or diffuse [73]. Second-order perturbation energy results derived from NBO analysis are widely utilized to assess hybridization, non-covalent interactions, and the overall stabilization of molecular systems.

 doi:10.20944/preprints202509.1018.v1

These results offer valuable insights into contributions from hyperconjugation, resonance, and other electron delocalization effects that impact the molecule's electronic structure and reactivity [74,75]. Table 9 presents the 2nd-order perturbative energy results for the TCC compound, as determined in this study. The most significant stabilization energy contributions arise from the following electron delocalization interactions: LP(1) O23 → *πO14–C6* (50.05 kcal mol^{-1}), *LP(1) O25* → πC13–O26 (45.21 kcal mol^{-1}), and LP(1) O26 → *πC32–O15* (36.58 kcal mol^{-1}). These interactions represent major resonance effects that enhance the stability of the TCC molecule. Additionally, electron delocalization from the lone pair on N37 to the antibonding orbital πS54–N37 contributes 13.19 kcal mol^{-1} to stabilization energy. In summary, the TCC compound exhibits the highest second-order perturbation energy (E^2), indicating a substantial contribution to electronic stabilization and, consequently, an enhanced corrosion inhibition efficiency compared to other inhibitors.

Table 9. Second-order perturbation theory analysis of Fock Matrix in NBO Basis of TCC compound at B3LYP/6-311++G (d, p) level in the gas phase.

Compound	Donor	Acceptor	$E^{(2)a}$(kcal/mol)	Occupancy
TCC	πC12–O41	π*C13–O40	22.52	1.67
	πC19–O15	π*C11–C13	21.13	1.65
	LP (1) N37	π*S54–N37	13.19	1.87
	LP (1) O23	π*O14–C6	50.05	1.74
	LP (1) O24	π*O23–O15	16.74	1.75
	LP (1) O25	π*C13–O26	45.21	1.88
	LP (1) O26	π*C32–O15	36.58	1.69
	LP (1) O27	π*C10–O24	26.47	1.57
	LP (3) S54	π*O14–N37	31.04	1.35
	LP (2) O14	π*S54–H57	29.83	1.82
	LP (2) O15	π*C10–C7	18.81	1.94
	LP (2) O16	π*C13–C11	28.83	1.82
	LP (2) O53	π*C13–O16	19.81	1.94
	LP (2) O41	π*C10–O15	33.04	1.37

3.7.2. Molecular Simulation Dynamics

The adsorption behavior of the TCC inhibitor on the 101 ASS surface was investigated using molecular dynamics (MD) simulations. In the absence of solvent molecules, the interaction between the TCC molecule and the surface of Ti alloy (101) was examined within an isolated interactive system. The interaction energy ($E_{\_interaction}$) and binding energy ($E_{\_binding}$) of the created system were estimated using the following equations [76].

$$E_{interaction} = E_{total} - (E_{surface\ +\ solution} - E_{inhibitor}) \quad (11)$$

$$E_{bindi} = -E_{interaction} \quad (12)$$

Where $E_{inhibitor}$ denotes the energy of an inhibitor molecule, and E_{total} denotes the total energy of the entire system under study, $E_{surface\ +\ solution}$ denotes the total energy of the Ti (101) surface and solution without TCC inhibitor.

Figure 17 illustrates the use of the Layer Builder to position the TCC on the surface of Ti (101). For TCC, the calculated interaction energy was −763.27 kcal·mol^{-1}, while the binding energy was found to be 763.27 kcal mol^{-1}. As presented in Figure 18, the TCC inhibitor adsorbs in a parallel orientation to the Ti (101) alloy surface, achieving maximum surface coverage through interactions involving the π-electrons of aromatic rings, as well as oxygen, nitrogen, and sulfur atoms. These interactions result in strong adsorption, thereby enhancing the inhibition efficiency [77].

The chemical bonding between the TCC molecule and the Ti6Al4V surface of the 101 ASS was inspected using the radial distribution function (RDF) method [78–80]. Chemisorption is indicated by peaks appearing at distances of approximately 1 Å and 3.5 Å, while peaks beyond 3.5 Å correspond to physisorption [77]. As shown in Figure 19, the first obvious peak, seen at fewer than

 doi:10.20944/preprints202509.1018.v1

3.5 Å, suggests the foundation of chemical bonds between TCC and Ti atoms. Moreover, the presence of peaks past 3.5 Å is attributed to physical interactions. The TCC inhibitor demonstrates a high capacity for donating and accepting electrons via active sites, which facilitates its adsorption onto the Ti6Al4V (101 ASS) surface and provides protection against dissolution. Our findings indicate that the TCC inhibitor exhibits mixed adsorption behavior, having both chemisorption and physisorption, as revealed by the RDF analysis. Furthermore, there is strong agreement between surface analysis, theoretical studies, molecular dynamics (MD) simulations, RDF results, and experimental measurements.

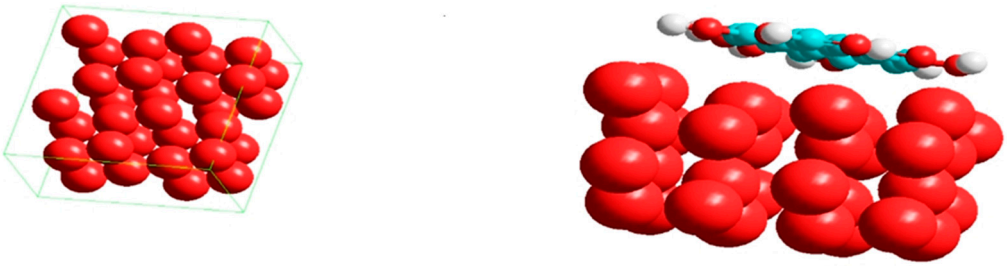

Figure 17. The Layer Builder to place the TCC inhibitor on the Ti6Al4V (1 0 1) surface.

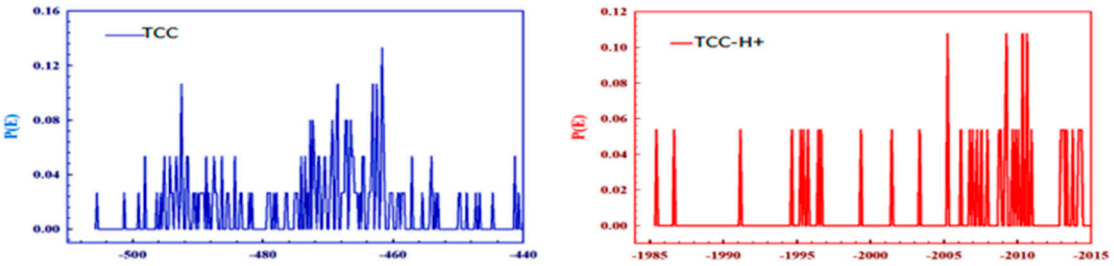

Figure 18. Adsorption energy distribution for the most suitable configuration of adsorption obtained for TCC and $TCCH^+$ on the Ti6Al4V (1 0 1) surface in the gas phase at 298 K.

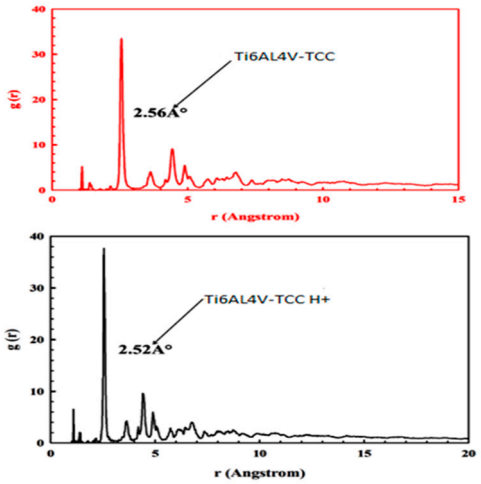

Figure 19. Radial distribution functions of adsorbed TCC and $TCCH^+$ on the Ti6Al4V (1 0 1) substrate by an adsorption locator module.

 doi:10.20944/preprints202509.1018.v1

5. Conclusions

The current study used a variety of electrochemical techniques to investigate and assess the TCC's adsorption and mitigation capacity in SS. Additionally, various surface analysis techniques were applied to examine the surface morphology of Ti6Al4V alloys both before and after the addition of TCC inhibitor. Additionally, DFT, MD, and NOB were employed to assess the correlation between the experimental work and theoretical quantum investigation, aiming to explain the relationship between the molecular/electronic structure of TCC and its effectiveness in inhibition.

Based on the data collected, the outcomes that follow can be drawn:

1. The TCC inhibitor's activity increased with an elevation in its concentration (reaching 92.40% when 200 mg/l of TCC was used) and reduced with a temperature rise.
2. The mitigation power of the TCC can be clarified by its physical adsorption onto the Ti6A14V surface, which follows the Langmuir adsorption model.
3. When TCC is present at 200 mg/l, the polarization resistance (R_P) rises from 7.85 kΩ cm^2 for the blank solution to 78.88 kΩ cm^2.
4. The apparent activation energy of the corrosion is higher in the presence of TCC (35.79 kJ mol^{-1}) than in its absence (14.46 kJ mol^{-1}).
5. Several techniques, such as AFM, CA, SEM, and UV-visible, were used to confirm the TCC adsorption and formation of a protective film on the Ti-alloy.
6. The parameters derived from quantum chemical calculations (DFT), molecular dynamics simulations (MD), and NOB agreed well with the experimental data.

Author Contributions: I.M.A.O.: Conceptualization, Data curation, Writing—original draft, Writing—review & editing, Investigation, Formal analysis, Methodology. **I. H. El..:** Conceptualization, Data curation, Writing—original draft, Writing—review & editing, Visualization, Investigation, Formal analysis, Methodology. **S. A. El.** Conceptualization, Visualization, Investigation, Formal analysis, Methodology, Writing—review & editing, Visualization. **M.A.M.I.:** Conceptualization, Data curation, Writing—original draft, Writing—review & editing, Visualization, Investigation. All authors have read and agreed to the published version of the manuscript.

Funding: This research received no external funding.

Data Availability Statement: All data generated or analyzed during this study are included in this published article.

Conflicts of Interest: The authors declare that they have no competing interests.

References

1. Cvijović-Alagić, I.; Cvijović, Z.; Bajat, J.; Rakin, M., Composition and processing effects on the electrochemical characteristics of biomedical titanium alloys. *Corrosion Science* 2014, *83*, 245-254. https://doi.org/10.1016/j.corsci.2014.02.017
2. Su, C.; Yu, H.; Wang, Z.; Yang, J.; Zeng, X., Controlling the tensile and fatigue properties of selective laser melted Ti–6Al–4V alloy by post treatment. *Journal of Alloys and Compounds* 2021, *857*, 157552. https://doi.org/10.1016/j.jallcom.2020.157552
3. Okazaki, Y.; Tateishi, T.; Ito, Y., Corrosion resistance of implant alloys in pseudo physiological solution and role of alloying elements in passive films. *Materials Transactions, JIM* 1997, *38* (1), 78-84. https://doi.org/10.2320/matertrans1989.38.78
4. Tsai, M.-T.; Chen, Y.-W.; Chao, C.-Y.; Jang, J. S.; Tsai, C.-C.; Su, Y.-L.; Kuo, C.-N., Heat-treatment effects on mechanical properties and microstructure evolution of Ti-6Al-4V alloy fabricated by laser powder bed fusion. *Journal of Alloys and Compounds* 2020, *816*, 152615. https://doi.org/10.1016/j.jallcom.2019.152615

 doi:10.20944/preprints202509.1018.v1

5. Choi, Y. R.; Sun, S. D.; Liu, Q.; Brandt, M.; Qian, M., Influence of deposition strategy on the microstructure and fatigue properties of laser metal deposited Ti-6Al-4V powder on Ti-6Al-4V substrate. *International Journal of Fatigue* 2020, *130*, 105236. https://doi.org/10.1016/j.ijfatigue.2019.105236
6. Zhou, X.; Leng, A.; Li, C.; Tang, T.; Xu, J.; Wei, B.; Liao, B.; Sun, C., The role of oral microbiota in accelerating corrosion of Ti6Al4V: An electrochemical study. *Materials Chemistry and Physics* 2025, *340*, 130836. https://doi.org/10.1016/j.matchemphys.2025.130836
7. Torbati-Sarraf, H.; Ding, L.; Khakpour, I.; Daviran, G.; Poursaee, A., Unraveling the corrosion of the Ti–6Al–4V orthopedic alloy in phosphate-buffered saline (PBS) solution: Influence of frequency and potential. *Corrosion and Materials Degradation* 2024, *5* (2), 276-288. https://doi.org/10.3390/cmd5020012
8. Yu, F.; Addison, O.; Davenport, A. J., A synergistic effect of albumin and H2O2 accelerates corrosion of Ti6Al4V. *Acta biomaterialia* 2015, *26*, 355-365. https://doi.org/10.1016/j.actbio.2015.07.046
9. Raghavendra, G. M.; Varaprasad, K.; Jayaramudu, T., Biomaterials: design, development and biomedical applications. In *Nanotechnology applications for tissue engineering*, Elsevier: 2015; pp 21-44. https://doi.org/10.1016/B978-0-323-32889-0.00002-9
10. Boraei, N. F. E.; Ibrahim, M. A.; Rehim, S. S. A. E.; Elshamy, I. H., Electrochemical corrosion behavior of β-Ti alloy in a physiological saline solution and the impact of H2O2 and albumin. *Journal of Solid State Electrochemistry* 2024, *28* (7), 2243-2256. https://doi.org/10.1007/s10008-023-05751-z
11. Boraei, N. F. E.; Elshamy, I. H.; Ibrahim, M. A., A comparative study on the electrochemical corrosion behaviour of biomedical β-titanium alloy with TiAlV and titanium in hank's physiological solution and the impact of reactive oxygen species and immersion time. *Journal of Bio-and Tribo-Corrosion* 2024, *10* (2), 38. https://doi.org/10.1007/s40735-024-00839-z
12. Shivaram, M.; Arya, S. B.; Nayak, J.; Panigrahi, B. B., Electrochemical Corrosion and Impedance Studies of Porous Ti–x Nb–Ag Alloy in Physiological Solution. *Transactions of the Indian Institute of Metals* 2020, *73*, 921-928. https://doi.org/10.1007/s12666-020-01904-0
13. El Boraei, N. F.; Ibrahim, M. A.; El Rehim, S. S. A.; Elshamy, I. H., The Effect of Annealing Temperature and Immersion Time on the Active–Passive Dissolution of Biomedical Ti70Zr20Nb7. 5Ta2. 5 Alloy in Ringer's Solution. *Journal of Bio-and Tribo-Corrosion* 2023, *9* (3), 62. https://doi.org/10.1007/s40735-023-00779-0
14. Höhn, S.; Braem, A.; Neirinck, B.; Virtanen, S., Albumin coatings by alternating current electrophoretic deposition for improving corrosion resistance and bioactivity of titanium implants. *Materials Science and Engineering: C* 2017, *73*, 798-807. https://doi.org/10.1016/j.msec.2016.12.129
15. González, J.; Mirza-Rosca, J., Study of the corrosion behavior of titanium and some of its alloys for biomedical and dental implant applications. *Journal of Electroanalytical Chemistry* 1999, *471* (2), 109-115. https://doi.org/10.1016/S0022-0728(99)00260-0
16. Heakal, F. E.-T.; Ghoneim, A.; Mogoda, A.; Awad, K., Electrochemical behaviour of Ti–6Al–4V alloy and Ti in azide and halide solutions. *Corrosion science* 2011, *53* (9), 2728-2737. https://doi.org/10.1016/j.corsci.2011.05.003
17. Qu, Q.; Wang, L.; Chen, Y.; Li, L.; He, Y.; Ding, Z., Corrosion behavior of titanium in artificial saliva by lactic acid. *Materials* 2014, *7* (8), 5528-5542. https://doi.org/10.3390/ma7085528
18. Mareci, D.; Ungureanu, G.; Aelenei, D.; Rosca, J. M., Electrochemical characteristics of titanium based biomaterials in artificial saliva. *Materials and Corrosion* 2007, *58* (11), 848-856. https://doi.org/10.1002/maco.200704065
19. Elshamy, I. H.; Ibrahim, M. A.; Abdel Rehim, S. S.; El Boraei, N. F., Electrochemical characteristics of a biomedical Ti70Zr20Nb7. 5Ta2. 5 refractory high entropy alloy in an artificial saliva solution. *Journal of Bio-and Tribo-Corrosion* 2023, *9* (1), 10. https://doi.org/10.1007/s40735-022-00726-5

 doi:10.20944/preprints202509.1018.v1

20. Barril, S.; Mischler, S.; Landolt, D., Electrochemical effects on the fretting corrosion behaviour of Ti6Al4V in 0.9% sodium chloride solution. *Wear* 2005, *259* (1-6), 282-291. https://doi.org/10.1016/j.wear.2004.12.012
21. Cao, L.; Wan, Y.; Yang, S.; Pu, J., The tribocorrosion and corrosion properties of thermally oxidized Ti6Al4V alloy in 0.9 wt.% NaCl physiological saline. *Coatings* 2018, *8* (8), 285. https://doi.org/10.3390/coatings8080285
22. Hrir, H.; Ait Layachi, O.; Boudouma, A.; El Bouari, A.; Ait Sidimou, A.; El Marrakchi, M.; Khoumri, E., Electrochemical corrosion behavior of α-titanium alloys in simulated biological environments (comparative study). *RSC advances* 2024, *14* (51), 38110-38119. https://doi.org/10.1039/D4RA05869K
23. Li, L.; Feng, Y.; Liu, Y.; Wei, B.; Guo, J.; Jiao, W.; Zhang, Z.; Zhang, Q., Titanium dioxide nanoparticles modified by salicylic acid and arginine: Structure, surface properties and photocatalytic decomposition of p-nitrophenol. *Applied Surface Science* 2016, *363*, 627-635. https://doi.org/10.1016/j.apsusc.2015.12.044
24. Almashhadani, H. A.; Alshujery, M. K.; Khalil, M.; Kadhem, M. M.; Khadom, A. A., Corrosion inhibition behavior of expired diclofenac Sodium drug for Al 6061 alloy in aqueous media: Electrochemical, morphological, and theoretical investigations. *Journal of Molecular Liquids* 2021, *343*, 117656. https://doi.org/10.1016/j.molliq.2021.117656
25. Hamza, M.; Abd El Rehim, S.; Ibrahim, M. A., Inhibition effect of hexadecyl pyridinium bromide on the corrosion behavior of some austenitic stainless steels in H2SO4 solutions. *Arabian Journal of Chemistry* 2013, *6* (4), 413-422. https://doi.org/10.1016/j.arabjc.2010.11.002
26. Abd El Rehim, S.; Ibrahim, M. A.; Khalid, K., The inhibition of 4-(2′-amino-5′-methylphenylazo) antipyrine on corrosion of mild steel in HCl solution. *Materials Chemistry and Physics* 2001, *70* (3), 268-273. https://doi.org/10.1016/S0254-0584(00)00462-4
27. Nathiya, R.; Perumal, S.; Murugesan, V.; Raj, V., Expired drugs: environmentally safe inhibitors for aluminium corrosion in 1 M H2SO4. *Journal of Bio-and Tribo-Corrosion* 2018, *4* (1), 4. https://doi.org/10.1007/s40735-017-0120-1
28. Schmitt, G., Application of inhibitors for acid media: report prepared for the European federation of corrosion working party on inhibitors. *British Corrosion Journal* 1984, *19* (4), 165-176. https://doi.org/10.1179/000705984798273100
29. Sastri, V. S., *Corrosion inhibitors: principles and applications*. Wiley New York: 1998; Vol. 1. https://doi.org/10.1108/acmm.2002.12849cae.001
30. Ibrahim, M. A.; Elshamy, I. H.; Elshamy, M. I.; Elaraby, A., An experimental and computational investigation on the performance of cefotaxime in mitigating Ti6Al4V alloy corrosion. *Corrosion Engineering, Science and Technology* 2025, 1478422X251348976. https://doi.org/10.1177/1478422X251348976
31. Onyeachu, I. B.; Abdel-Azeim, S.; Chauhan, D. S.; Quraishi, M. A., Electrochemical and computational insights on the application of expired Metformin drug as a novel inhibitor for the sweet corrosion of C1018 steel. *ACS omega* 2020, *6* (1), 65-76. https://dx.doi.org/10.1021/acsomega.0c03364?ref=pdf
32. Karthikeyan, S., Drugs/antibiotics as potential corrosion inhibitors for metals—a review. *International Journal of ChemTech Research* 2016, *9* (6), 251-259.
33. Abdallah, M.; Alfakeer, M.; El Guesmi, N.; Felaly, R. N.; Al-Juaid, S. S.; Al-abdali, F. H.; Sobhi, M., Appraisal of expired linezolid and piperacillin as potent and harmless inhibitors for mitigation of copper corrosion in 1.0 M HNO3. *Green Chemistry Letters and Reviews* 2025, *18* (1), 2474131. https://doi.org/10.1080/17518253.2025.2474131
34. Radovanović, M. B.; Tasić, Z. a. Z.; Simonović, A. T.; Petrović Mihajlović, M. B.; Antonijević, M. M., Corrosion behavior of titanium in simulated body solutions with the addition of biomolecules. *ACS omega* 2020, *5* (22), 12768-12776. http://pubs.acs.org/journal/acsodf?ref=pdf

 doi:10.20944/preprints202509.1018.v1

35. Abdallah, M.; Al-Rashidi, A.; Al-Gorair, A. S.; Al-Juaid, S. S.; Soliman, K. A., Experimental and theoretical analysis of expired doxycycline and Klacid as aluminum corrosion inhibitors in HCl. *Corrosion Engineering, Science and Technology* 2024, 1478422X251351692. https://doi.org/10.1177/1478422X251351692
36. Kotabagi, S. D.; Rajappa, S.; Minagalavar, R. L.; Rathod, M. R.; Suma, J.; Sajjan, A. M., Expired Lircetam drug as a corrosion inhibitor for low-carbon steel in 1 M HCl: Experimental, theoretical, and quantum chemical insights. *Results in Surfaces and Interfaces* 2025, *18*, 100459. https://doi.org/10.1016/j.rsurfi.2025.100459
37. Gece, G., Drugs: A review of promising novel corrosion inhibitors. *Corrosion science* 2011, *53* (12), 3873-3898. https://doi.org/10.1016/j.corsci.2011.08.006
38. Bhamburkar, S.; Khandare, S.; Patharkar, S.; Thakare, S., Thiocolchicoside: an updated review. 2022. http://dx.doi.org/10.52711/2231-5659.2022.00038
39. Soonawalla, D. F.; Joshi, N., Efficacy of thiocolchicoside in Indian patients suffering from low back pain associated with muscle spasm. *Journal of the Indian Medical Association* 2008, *106* (5), 331-335.
40. Ketenci, A.; Ozcan, E.; Karamursel, S., Assessment of efficacy and psychomotor performances of thiocolchicoside and tizanidine in patients with acute low back pain. *International journal of clinical practice* 2005, *59* (7), 764-770. https://doi.org/10.1111/j.1742-1241.2004.00454.x
41. El-Mokadem, T.; Hashem, A.; Abd El-Sattar, N. E.; Dawood, E.; Abdelshafi, N., Green synthesis, electrochemical, DFT studies and MD simulation of novel synthesized thiourea derivatives on carbon steel corrosion inhibition in 1.0 M HCl. *Journal of Molecular Structure* 2023, *1274*, 134567. https://doi.org/10.1016/j.molstruc.2022.134567
42. Abdelshafi, N.; Farag, A. A.; Heakal, F. E.-T.; Badran, A.-S.; Abdel-Azim, K.; El Sayed, A.-R. M.; Ibrahim, M. A., In-depth experimental assessment of two new aminocoumarin derivatives as corrosion inhibitors for carbon steel in HCl media combined with AFM, SEM/EDX, contact angle, and DFT/MDs simulations. *Journal of Molecular Structure* 2024, *1304*, 137638. https://doi.org/10.1016/j.molstruc.2024.137638
43. Hadisaputra, S.; Purwoko, A. A.; Savalas, L. R. T.; Prasetyo, N.; Yuanita, E.; Hamdiani, S., Quantum chemical and Monte Carlo simulation studies on inhibition performance of caffeine and its derivatives against corrosion of copper. *Coatings* 2020, *10* (11), 1086. https://doi.org/10.3390/coatings10111086
44. Arrousse, N.; Salim, R.; Kaddouri, Y.; Zahri, D.; El Hajjaji, F.; Touzani, R.; Taleb, M.; Jodeh, S., The inhibition behavior of two pyrimidine-pyrazole derivatives against corrosion in hydrochloric solution: Experimental, surface analysis and in silico approach studies. *Arabian Journal of Chemistry* 2020, *13* (7), 5949-5965. https://doi.org/10.1016/j.arabjc.2020.04.030
45. Cao, Z.; Tang, Y.; Cang, H.; Xu, J.; Lu, G.; Jing, W., Novel benzimidazole derivatives as corrosion inhibitors of mild steel in the acidic media. Part II: Theoretical studies. *Corrosion Science* 2014, *83*, 292-298. https://doi.org/10.1016/j.corsci.2014.02.025
46. Khaled, K.; Hamed, M. N.; Abdel-Azim, K.; Abdelshafi, N., Inhibition of copper corrosion in 3.5% NaCl solutions by a new pyrimidine derivative: electrochemical and computer simulation techniques. *Journal of Solid State Electrochemistry* 2011, *15* (4), 663-673. https://doi.org/10.1007/s10008-010-1110-0
47. Pinto, G. M.; Nayak, J.; Shetty, A. N., Corrosion inhibition of 6061 Al–15 vol. pct. SiC (p) composite and its base alloy in a mixture of sulphuric acid and hydrochloric acid by 4-(N, N-dimethyl amino) benzaldehyde thiosemicarbazone. *Materials Chemistry and Physics* 2011, *125* (3), 628-640. https://doi.org/10.1016/j.matchemphys.2010.10.006
48. Zhang, X.; Li, W.; Zuo, X.; Tan, B.; Xu, C.; Zhang, S., Investigating the inhibitive effect of Davidia involucrata leaf extract as a biological eco-friendly inhibitor for copper in acidic medium. *Journal of Molecular Liquids* 2021, *325*, 115214. https://doi.org/10.1016/j.molliq.2020.115214

49. Chocholoušová, J.; Špirko, V.; Hobza, P., First local minimum of the formic acid dimer exhibits simultaneously red-shifted O–H⋯ O and improper blue-shifted C–H⋯ O hydrogen bonds. *Physical Chemistry Chemical* Physics 2004, *6* (1), 37-41. https://doi.org/10.1039/B314148A
50. Szafran, M.; Komasa, A.; Bartoszak-Adamska, E., Crystal and molecular structure of 4-carboxypiperidinium chloride (4-piperidinecarboxylic acid hydrochloride). *Journal of molecular structure* 2007, *827* (1-3), 101-107. DOI:10.1016/j.molstruc.2006.05.012.
51. Yadav, D. K.; Chauhan, D.; Ahamad, I.; Quraishi, M., Electrochemical behavior of steel/acid interface: adsorption and inhibition effect of oligomeric aniline. *RSC advances* 2013, *3* (2), 632-646. https://doi.org/10.1039/C2RA21697C
52. Yadav, D. K.; Quraishi, M., Electrochemical investigation of substituted pyranopyrazoles adsorption on mild steel in acid solution. *Industrial & engineering chemistry research* 2012, *51* (24), 8194-8210. https://doi.org/10.1021/ie3002155
53. Becke, A. D., Density-functional thermochemistry. III. The role of exact exchange. *The Journal of chemical physics* 1993, *98* (7), 5648-5652. https://doi.org/10.1063/1.464913
54. Dunning Jr, T. H., Gaussian basis sets for use in correlated molecular calculations. I. The atoms boron through neon and hydrogen. *The Journal of chemical physics* 1989, *90* (2), 1007-1023. https://doi.org/10.1063/1.456153
55. Espinoza-Vázquez, A.; Rodríguez-Gómez, F.; González-Olvera, R.; Angeles-Beltrán, D.; Mendoza-Espinosa, D.; Negrón-Silva, G., Electrochemical assessment of phenol and triazoles derived from phenol (BPT) on API 5L X52 steel immersed in 1 M HCl. *RSC Advances* 2016, *6* (77), 72885-72896.
56. Verma, C.; Quraishi, M. A.; Kluza, K.; Makowska-Janusik, M.; Olasunkanmi, L. O.; Ebenso, E. E., Corrosion inhibition of mild steel in 1M HCl by D-glucose derivatives of dihydropyrido [2, 3-d: 6, 5-d'] dipyrimidine-2, 4, 6, 8 (1H, 3H, 5H, 7H)-tetraone. *Scientific Reports* 2017, *7* (1), 44432. https://doi.org/10.1038/srep44432
57. Hrimla, M.; Bahsis, L.; Boutouil, A.; Laamari, M. R.; Julve, M.; Stiriba, S.-E., Corrosion inhibition performance of a structurally well-defined 1, 2, 3-triazole derivative on mild steel-hydrochloric acid interface. *Journal of Molecular Structure* 2021, *1231*, 129895. https://doi.org/10.1016/j.molstruc.2021.129895
58. Olasunkanmi, L. O.; Kabanda, M. M.; Ebenso, E. E., Quinoxaline derivatives as corrosion inhibitors for mild steel in hydrochloric acid medium: Electrochemical and quantum chemical studies. *Physica E: Low-dimensional Systems and Nanostructures* 2016, *76*, 109-126. https://doi.org/10.1016/j.physe.2015.10.005
59. Rouifi, Z.; Rbaa, M.; Abousalem, A. S.; Benhiba, F.; Laabaissi, T.; Oudda, H.; Lakhrissi, B.; Guenbour, A.; Warad, I.; Zarrouk, A., Synthesis, characterization and corrosion inhibition potential of newly benzimidazole derivatives: combining theoretical and experimental study. *Surfaces and Interfaces* 2020, *18*, 100442. https://doi.org/10.1016/j.surfin.2020.100442
60. Shalabi, K.; Abdel-Galil, E.; El-Askalany, A.; Abdallah, Y., Adsorption, electrochemical behavior, and theoretical studies for copper corrosion inhibition in 1 M nitric acid medium using triazine derivatives. *Journal of Molecular Liquids* 2022, *348*, 118420. https://doi.org/10.1016/j.molliq.2021.118420
61. Abdel-Gaber, A.; Khamis, E.; Abo-Eldahab, H.; Adeel, S., Novel package for inhibition of aluminium corrosion in alkaline solutions. *Materials Chemistry and Physics* 2010, *124* (1), 773-779. https://doi.org/10.1016/j.matchemphys.2010.07.059
62. Aouine, Y.; Sfaira, M.; Touhami, M. E.; Alami, A.; Hammouti, B.; Elbakri, M.; El Hallaoui, A.; Touir, R., Temperature and time investigations on the adsorption behavior of isoindoline, tetrazole and isoindoline-tetrazole on corrosion of mild steel in acidic medium. *International Journal of Electrochemical Science* 2012, *7* (6), 5400-5419. https://doi.org/10.1016/S1452-3981(23)19630-1

 doi:10.20944/preprints202509.1018.v1

63. Amin, M. A.; Ibrahim, M. M., Corrosion and corrosion control of mild steel in concentrated H2SO4 solutions by a newly synthesized glycine derivative. *Corrosion Science* 2011, *53* (3), 873-885. https://doi.org/10.1016/j.corsci.2010.10.022
64. Kokalj, A., Corrosion inhibitors: physisorbed or chemisorbed? *Corrosion Science* 2022, *196*, 109939. https://doi.org/10.1016/j.corsci.2021.109939
65. Fawzy, A.; Abdallah, M.; Zaafarany, I.; Ahmed, S.; Althagafi, I., Thermodynamic, kinetic and mechanistic approach to the corrosion inhibition of carbon steel by new synthesized amino acids-based surfactants as green inhibitors in neutral and alkaline aqueous media. *Journal of Molecular Liquids* 2018, *265*, 276-291. https://doi.org/10.1016/j.molliq.2018.05.140
66. Hegazy, M., Novel cationic surfactant based on triazole as a corrosion inhibitor for carbon steel in phosphoric acid produced by dihydrate wet process. *Journal of Molecular Liquids* 2015, *208*, 227-236. https://doi.org/10.1016/j.molliq.2015.04.042
67. Machnikova, E.; Whitmire, K. H.; Hackerman, N., Corrosion inhibition of carbon steel in hydrochloric acid by furan derivatives. *Electrochimica Acta* 2008, *53* (20), 6024-6032. https://doi.org/10.1016/j.electacta.2008.03.021
68. Saliyan, V. R.; Adhikari, A. V., Quinolin-5-ylmethylene-3-{[8-(trifluoromethyl) quinolin-4-yl] thio} propanohydrazide as an effective inhibitor of mild steel corrosion in HCl solution. *Corrosion Science* 2008, *50* (1), 55-61. https://doi.org/10.1016/j.corsci.2006.06.035
69. Rouifi, Z.; Rbaa, M.; Benhiba, F.; Laabaissi, T.; Oudda, H.; Lakhrissi, B.; Guenbour, A.; Warad, I.; Zarrouk, A., Preparation and anti-corrosion activity of novel 8-hydroxyquinoline derivative for carbon steel corrosion in HCl molar: computational and experimental analyses. *Journal of Molecular Liquids* 2020, *307*, 112923. https://doi.org/10.1016/j.molliq.2020.112923
70. Politzer, P.; Murray, J. S., The fundamental nature and role of the electrostatic potential in atoms and molecules. *Theoretical Chemistry Accounts* 2002, *108* (3), 134-142. https://doi.org/10.1007/s00214-002-0363-9
71. Abd El-Lateef, H. M.; Sayed, A. R.; Gomha, S. M.; Bakir, E. M.; Shalabi, K., Synthesis and study of poly [(hydrazinylazo)] thiazoles as potent corrosion inhibitors for cast iron-carbon alloy in molar HCl: A collective computational and experiential methods. *Journal of Molecular Liquids* 2021, *337*, 116555. https://doi.org/10.1016/j.molliq.2021.116555
72. Fouda, A.; Ismail, M.; Abousalem, A. S.; Elewady, G., Experimental and theoretical studies on corrosion inhibition of 4-amidinophenyl-2, 2′-bifuran and its analogues in acidic media. *Rsc Advances* 2017, *7* (73), 46414-46430. https://doi.org/10.1039/C7RA08092A
73. Mert, B. D.; Yüce, A. O.; Kardaş, G.; Yazıcı, B., Inhibition effect of 2-amino-4-methylpyridine on mild steel corrosion: experimental and theoretical investigation. *Corrosion science* 2014, *85*, 287-295. https://doi.org/10.1016/j.corsci.2014.04.032
74. Guerrab, W.; Chung, I.-M.; Kansiz, S.; Mague, J. T.; Dege, N.; Taoufik, J.; Salghi, R.; Ali, I. H.; Khan, M. I.; Lgaz, H., Synthesis, structural and molecular characterization of 2, 2-diphenyl-2H, 3H, 5H, 6H, 7H-imidazo [2, 1-b][1, 3] thiazin-3-one. *Journal of Molecular Structure* 2019, *1197*, 369-376. https://doi.org/10.1016/j.molstruc.2019.07.081
75. Guerrab, W.; Lgaz, H.; Kansiz, S.; Mague, J. T.; Dege, N.; Ansar, M.; Marzouki, R.; Taoufik, J.; Ali, I. H.; Chung, I.-M., Synthesis of a novel phenytoin derivative: crystal structure, Hirshfeld surface analysis and DFT calculations. *Journal of Molecular Structure* 2020, *1205*, 127630. https://doi.org/10.1016/j.molstruc.2019.127630
76. Abdallah, M.; Al Bahir, A.; Altass, H.; Fawzy, A.; El Guesmi, N.; Al-Gorair, A. S.; Benhiba, F.; Warad, I.; Zarrouk, A., Anticorrosion and adsorption performance of expired antibacterial drugs on Sabic iron

 doi:10.20944/preprints202509.1018.v1

corrosion in HCl solution: Chemical, electrochemical and theoretical approach. *Journal of Molecular Liquids* 2021, *330*, 115702. https://doi.org/10.1016/j.molliq.2021.115702

77. Abdelshafi, N.; Ibrahim, M. A.; Badran, A.-S.; Halim, S. A., Experimental and theoretical evaluation of a newly synthesized quinoline derivative as corrosion inhibitor for iron in 1.0 M hydrochloric acid solution. *Journal of Molecular Structure* 2022, *1250*, 131750. https://doi.org/10.1016/j.molstruc.2021.131750
78. Jucai, W.; Ke, T.; Xiaodi, S.; Xin, H., Theoretical calculations of pyridine adsorption on the surfaces of Ti, Zr, N doped graphene. *Journal of Fuel Chemistry and Technology* 2024, *52* (8), 1162-1172. https://doi.org/10.1016/S1872-5813(24)60440-8
79. Tshwane, D. M.; Modiba, R.; Govender, G.; Ngoepe, P.; Chauke, H., The adsorption of halogen molecules on Ti (110) surface. *Journal of Materials Research* 2021, *36*, 592-601. https://doi.org/10.1557/s43578-021-00106-8
80. Boda, A.; Chandorkar, N.; Ali, S. M., Density functional theoretical assessment of titanium metal for adsorption of hydrogen, deuterium and tritium isotopes. *Theoretical Chemistry Accounts* 2023, *142* (5), 46. https://doi.org/10.1007/s00214-023-02988-9